SECOND HARMONIC GENERATION IN SI/SIO2 SYSTEMS

By

Heungman Park

Dissertation

Submitted to the faculty of the

Graduate school of Vanderbilt University

in partial fulliment of the requirements

for the degree of

DOCTOR OF PHILOSOPHY

in

Physics

August 2010

Nashville, Tennessee

Approved:

Professor Norman H. Tolk

Professor Shane M. Hustson

Professor Thomas W. Kephart

Professor Kalman Varga

Professor Jimmy L. Davidson

To my family

ACKNOWLEDGEMENTS

I gratefully acknowledge helpful guidance and support of my advisor, Professor Norman Tolk. He is the most passionate scientist that I have ever met. His enthusiasm for research inspired me to be a passionate scientist. I also would like to thank my committee members; Prof. Kalman Varga, Prof. Shane Huston, Prof. Thomas Kepart, and Prof. Jim Davidson. Especially I would like to give a special thanks to Professor Varga in helping me to understand the underlying physics of my research.

I thank CMASS group members; Jingbo Qi, Tavis Wade, Justin Gregory, Andrew Steigerwald, Stephanie Gilbert, Ying Xu, Xiong Lu and Dongmin Seo. I would like to express a special appreciation to Dr. Anthony Hmelo and Dr. Bo-Kyung Choi in the VINSE lab for their helpful discussion and support.

I am grateful to Professor Bridget Rogers. She helped me to understand the most important basic properties of boron atoms in silicon substrates. I am also grateful to Professor Gunter Lüpke at the College of William and Mary. I had many discussions with him on the experiments and also on the theoretical works in second harmonic generation. Due to their assistance I could publish my first second harmonic generation paper to Applied Physics Letters. I would also like to express my appreciation to Professor James Dickerson and Professor Sharon Weiss. Thanks to them I started my first research project at Vanderbilt and published my first journal paper.

Also, I would like to thank the staff of Vanderbilt Physics Department; Donald Pickert, Jane Fall, Barbara Amann, Sandy Childress, Peggy Mcgowan, Sheila Warf, and John Kozub in the FEL. I could get through my Ph.D. work without a big problem due to their friendly help.

I wish to express my special gratitude to the people who helped me to come to Vanderbilt University; Prof. William Hetherington, Prof. Bill Warren and Prof. Yun-Shik Lee at Oregon State University, Rich Lindball in Corvallis, Prof. Cha-Hwan Oh at Hanyang University in Korea and my middle school teacher, Dong-Su Kim.

Financial support for my graduate studies was provided in part by the Graduate School and Physics Department of Vanderbilt University, and also by the Department of Energy (DOE) of the United States.

Finally I dedicate my thesis to my family for their love and unconditional support.

TABLE OF CONTENTS

Page

LIST OF TABLES

LIST OF FIGURES

CHAPTER I

SECOND HARMONIC GENERATION (SHG)

This chapter deals with the basic concepts of nonlinear optics, a brief history of second harmonic generation, and the nonlinear optical properties of silicon. Because nonlinear optical phenomena involve multi-photon processes, nonlinear optical experiments require intense light sources. As a result, nonlinear optics became an important part of optical science after the invention of the laser. Nonlinear optical processes are explained by higher order polarization components involving higher order susceptibilities.

1.1 Introduction to second harmonic generation

In conventional optics, induced polarization in a material is linearly proportional to an externally imposed electric field. Typically, the proportionality constant is expressed by the electric susceptibility χ. Thus the linear response is described by the equation,

$$P = \chi E, \tag{1.1}$$

where P is a polarization vector and E is an electric field vector. To make it more general, χ becomes a tensor expressed as a 3×3 matrix because the vector E has three components. Therefore the general form of (1.1) is

$$\begin{pmatrix} P_x \\ P_y \\ P_z \end{pmatrix} = \begin{pmatrix} \chi_{xx} & \chi_{xy} & \chi_{xz} \\ \chi_{yx} & \chi_{yy} & \chi_{yz} \\ \chi_{zx} & \chi_{zy} & \chi_{zz} \end{pmatrix} \begin{pmatrix} E_x \\ E_y \\ E_z \end{pmatrix}. \tag{1.2}$$

Here we assume that the optical properties of the material, such as refractive index and absorption coefficient, remain unchanged with respect to the external electric field

E. At a low intensity of light, this assumption is usually valid. However, after the invention of the laser, a new phenomenon was observed. When the incident light is very intense, light-matter interaction produces light with doubled frequency, a process which is called second harmonic generation (SHG). A power series expansion of χ can characterize the second harmonic generation and other nonlinear optical phenomena such as third harmonic generation and optical rectification. If χ is expanded with respect to the electric field E, equation (1.1) is expressed by

$$\begin{aligned} P &= \chi E \\ &= (\chi^{(1)} + \chi^{(2)}E + \chi^{(3)}E^2 + \cdots)E \\ &= \chi^{(1)}E + \chi^{(2)}E^2 + \chi^{(3)}E^3 + \cdots \\ &= P^{(1)} + P^{(2)} + P^{(3)} \cdots . \end{aligned} \tag{1.3}$$

The first order polarization $P^{(1)}$ is responsible for the linear optical properties of a material, $P^{(2)}$ is responsible for second harmonic generation, $P^{(3)}$ for third harmonic generation and etc. A simple equation expressing the second order polarization is

$$P^{(2)} = \chi^{(2)}E^2. \tag{1.4}$$

To get a specific expression for SHG, we assume that the incoming electric field with frequency ω may be expressed as

$$E(t) = Ee^{-i\omega t} + Ee^{i\omega t}. \tag{1.5}$$

The square of the electric field is

$$\begin{aligned} E^2(t) &= (Ee^{-i\omega t} + Ee^{i\omega t})^2 \\ &= 2EE^* + E^2(e^{-i2\omega t} + Ee^{i2\omega t}). \end{aligned} \tag{1.6}$$

The second-order polarization $P^{(2)}$ has 2ω terms which describe the doubled frequency. The intensity of the SHG signals is proportional to the square of the second order polarization which is given by

$$I(2\omega) \propto |P^{(2)}|^2 = |\chi^{(2)}E(\omega)^2|^2 = |\chi^{(2)}|^2 I(\omega)^2. \tag{1.7}$$

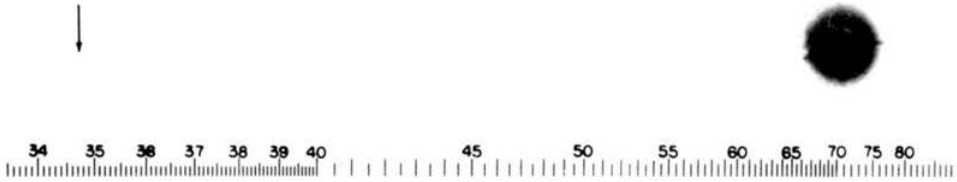

Figure 1.1: First spectroscopic measurement of second harmonic generation (SHG). The 694.3 nm wavelength beam from a ruby laser was used as the fundamental beam. SHG light was observed at a wavelength of 347.2 nm. The scale is in units of 10 nm [1]. A very weak signal was observed at approximately 347 nm (below the arrow) in the original manuscript.

The second-order susceptibility $\chi^{(2)}$ represents the second order material response to the incident light.

An exact relationship between the SHG beam intensity and fundamental beam intensity is determined by the material properties and the polarization configurations of the beams. For example, if the fundamental beam is incident onto a nonlinear medium 2 from a linear medium 1, the S-polarized SHG intensity $I_S^{(2\omega)}$ is given by [12, 13]

$$\begin{aligned} I_S^{(2\omega)} &= |E_S^{(2\omega)}|^2 \\ &= |\frac{i4\pi k_1}{k_{1z}+k_{2z}}\frac{k_1}{\epsilon_1}\ P_y^{(2)}|^2 \\ &= |\frac{i4\pi k_1}{k_{1z}+k_{2z}}\frac{k_1}{\epsilon_1}\ \chi^{(2)}E(\omega)^2|^2 \\ &= |\frac{i4\pi k_1}{k_{1z}+k_{2z}}\frac{k_1}{\epsilon_1}\ \chi^{(2)}I(\omega)|^2, \end{aligned} \tag{1.8}$$

where k_i and ϵ_i are wave vectors and dielectric constants at 2ω in medium 1 and 2 respectively, and $P_y^{(2)}$ is the perpendicular component of the second-order polarization vector in the media 2 with respect to the incident plane of the fundamental beam. The y component of the second order polarization $P_y^{(2)}$ is determined by the polarization status of the fundamental beam and $\chi^{(2)}$ of the nonlinear material.

This second order nonlinear optical phenomenon was reported experimentally after

the invention of the ruby laser in 1960. In 1961, the Weinreich group at the University of Michigan published the first SHG experimental result using a ruby laser ($\lambda = 694.3$ nm) with a quartz crystal [1]. They observed SHG light at $\lambda = 347.2$ nm which is the light of doubled frequency from the ruby laser which is described in Fig. 1.1.

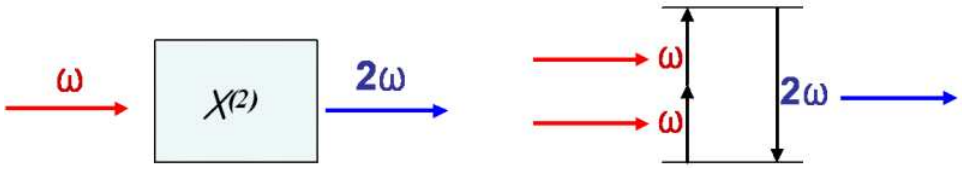

Figure 1.2: (a) left: simple description of second harmonic generation, (b) right: quantum mechanical description.

Figure 1.2(a) illustrates the principle of SHG. The SHG light with a 2ω frequency is generated by virtue of the second order susceptibility $\chi^{(2)}$ of a material. Second harmonic generation can be explained quantum mechanically by invoking electron energy level pseudo-states [14]. An electron can be excited from its ground state to a psuedo excited state by absorbing two photons with frequency ω, then the electron decays into the ground level by emitting a photon with 2ω frequency. Figure 1.2(b) shows the quantum mechanical description with a pseudo excited state and a ground state.

1.2 Classical anharmonic oscillator model for second harmonic generation

The linear optical responses of a material are explained by a harmonic potential model of the bound electrons in a solid. Classically SHG can be derived from an anharmonic oscillator model by expanding the harmonic potential model [15]. The potential of the bound electrons can be expanded as

$$U(x) = \frac{1}{2} m_0 \omega_0 x^2 + \frac{1}{3} m_0 C_3 x^3 + \cdots . \tag{1.9}$$

The equation of motion is

$$m_0\frac{d^2x}{dt^2} + m_0\gamma\frac{dx}{dt} + m_0C_3x^2 = -eE_0\frac{1}{2}(e^{-i\omega t} + Ee^{i\omega t}), \tag{1.10}$$

where γ is the damping term and the driving force is the external electric field E_0. The solution is assumed to be

$$x = \frac{1}{2}(X_1e^{i\omega t} + X_2e^{i2\omega t} + c.c.), \tag{1.11}$$

where $X_1 >> X_2$. From the equation of motion, we can obtain X_1, X_2 as

$$\begin{aligned} X_1 &= \frac{-eE_0}{m_0[(\omega_0^2 - \omega^2) + i\gamma\omega]}, \\ X_2 &= \frac{-C_3X_1^2}{2(\omega_0^2 - 4\omega^2 + 2i\gamma\omega)}. \end{aligned} \tag{1.12}$$

Finally, the susceptibilities are found to be

$$\chi^{(1)} = \frac{e^2}{m_0\epsilon_0[(\omega_0^2 - \omega^2) + i\gamma\omega]} \tag{1.13}$$

and

$$\chi^{(2)} = \frac{m_0C_3{\chi_{(\omega)}^{(1)}}^2\chi_{(2\omega)}^{(1)}\epsilon_0^2}{e^3}. \tag{1.14}$$

As shown in (1.14), the second-order susceptibility ($\chi^{(2)}$) is coupled with the first order susceptibilities ($\chi_{(\omega)}^{(1)}$, $\chi_{(2\omega)}^{(1)}$). Therefore if a material shows a strong linear optical response, it shows also strong nonlinear optical responses.

1.3 Second harmonic generation in silicon

The crystalline structure of silicon is diamond-cubic which has inversion symmetry. If there is inversion symmetry in a material, electric field and polarization vectors should be invariant under the inversion of the coordinate system. This means that if the coordinate system is changed by $r \to -r$, electric vector and polarization vector should be changed in the same manner, i.e. $E \to -E$ and $P^{(2)} = -P^{(2)}$. Therefore the

second order polarization equation (1.4), $P^{(2)} = \chi^{(2)}E^2$, holds the following relations under the inversion symmetry of the coordinate system.

$$\begin{aligned} -P^{(2)} &= \chi^{(2)}(-E)(-E) \\ &= \chi^{(2)}EE \\ &= P^{(2)}. \end{aligned} \tag{1.15}$$

Generally $P^{(2)}$ and $-P^{(2)}$ can be equal only if the $\chi^{(2)}$ vanishes. Therefore the second order susceptibility of bulk silicon is zero, i.e.

$$\chi^{(2)}_{bulk} = 0. \tag{1.16}$$

This result holds for any inversion symmetric materials such as silicon, diamond, germanium and amorphous SiO2. Thus in inversion symmetric materials SHG does not occur under the dipole radiation approximation. However inversion symmetric materials can generate SHG from higher order nonlinear responses such as magnetic dipole and electronic quadrupole responses [12]. In addition to the higher order nonlinear contribution, there is another source of SHG from silicon. At the surface of silicon, inversion symmetry is broken along the surface normal direction. Thus silicon (this is true of any material) has a non-vanishing second order surface susceptibility, $\chi^{(2)}_{surface}$. Typically the surface dipole contribution is dominant for silicon. A general expression of the second order surface polarization is given by

$$P^{(2)}_{surface} = \chi^{(2)}_{surface}E^2. \tag{1.17}$$

Equation (1.4) has three second order polarization vector components, 27 second order susceptibility components and 9 electric field components. It is expressed by

$$\begin{pmatrix} P_x^{(2)} \\ P_y^{(2)} \\ P_z^{(2)} \end{pmatrix} = \begin{pmatrix} \chi_{xxx} & \chi_{xxy} & \chi_{xxz} & \chi_{xyx} & \chi_{xyy} & \chi_{xyz} & \chi_{xzx} & \chi_{xzy} & \chi_{xzz} \\ \chi_{yxx} & \chi_{yxy} & \chi_{yxz} & \chi_{yyx} & \chi_{yyy} & \chi_{yyz} & \chi_{yzx} & \chi_{yzy} & \chi_{yzz} \\ \chi_{zxx} & \chi_{zxy} & \chi_{zxz} & \chi_{zyx} & \chi_{zyy} & \chi_{zyz} & \chi_{zzx} & \chi_{zzy} & \chi_{zzz} \end{pmatrix} \begin{pmatrix} E_xE_x \\ E_xE_y \\ E_xE_z \\ E_yE_x \\ E_yE_y \\ E_yE_z \\ E_zE_x \\ E_zE_y \\ E_zE_z \end{pmatrix}. \tag{1.18}$$

However, this equation has many redundant terms. For example, we can replace E_iE_j by E_jE_i. Thus it may be reduced into a more simple form as

$$\begin{pmatrix} P_x^{(2)} \\ P_y^{(2)} \\ P_z^{(2)} \end{pmatrix} = \begin{pmatrix} \chi_{xxx} & \chi_{xyy} & \chi_{xzz} & \chi_{xyz} & \chi_{xxz} & \chi_{xxy} \\ \chi_{yxx} & \chi_{yyy} & \chi_{yzz} & \chi_{yyz} & \chi_{yxz} & \chi_{yxy} \\ \chi_{zxx} & \chi_{zyy} & \chi_{zzz} & \chi_{zyz} & \chi_{zxz} & \chi_{zxy} \end{pmatrix} \begin{pmatrix} E_xE_x \\ E_yE_y \\ E_zE_z \\ 2E_yE_z \\ 2E_xE_z \\ 2E_xE_y \end{pmatrix}. \tag{1.19}$$

Not taking into account symmetry at the surface of silicon, the $\chi^{(2)}_{surface}$ term has 18 independent components. However there are inversion symmetries on the surface of silicon (or any cubic materials). Inversion symmetry is broken only in the normal direction. Therefore the tensor components of $\chi^{(2)}$ as expressed in equation (1.19) can be reduced by a symmetry analysis. For example, if the x and y axes are on the

surface plane of silicon (a cubic material) and the z axis is along the surface normal, we can apply mirror symmetry through the x axis. In this case, the x components of the polarization vector and the electric field vector of equation (1.19) are related as $P_x \to -P_x$ and $E_x \to -E_x$. If we consider the case where $E = (E_x, 0, 0)$, equation (1.19) becomes

$$\begin{pmatrix} P_x^{(2)} \\ P_y^{(2)} \\ P_z^{(2)} \end{pmatrix} = \begin{pmatrix} \chi_{xxx} & \chi_{xyy} & \chi_{xzz} & \chi_{xyz} & \chi_{xxz} & \chi_{xxy} \\ \chi_{yxx} & \chi_{yyy} & \chi_{yzz} & \chi_{yyz} & \chi_{yxz} & \chi_{yxy} \\ \chi_{zxx} & \chi_{zyy} & \chi_{zzz} & \chi_{zyz} & \chi_{zxz} & \chi_{zxy} \end{pmatrix} \begin{pmatrix} E_x E_x \\ 0 \\ 0 \\ 0 \\ 0 \\ 0 \end{pmatrix}. \tag{1.20}$$

Simply,

$$\begin{pmatrix} P_x^{(2)} \\ P_y^{(2)} \\ P_z^{(2)} \end{pmatrix} = \begin{pmatrix} \chi_{xxx} E_x E_x \\ \chi_{yxx} E_x E_x \\ \chi_{zxx} E_x E_x \end{pmatrix}. \tag{1.21}$$

Now if we apply inversion symmetry through the x-axis: $P_x \to -P_x$ and $E_x \to -E_x$, the x componet of equation (1.21) is

$$\begin{aligned} -P_x^{(2)} &= \chi_{xxx}(-E_x)(-E_x) \\ &= \chi_{xxx} E_x E_x \\ &= P_x^{(2)}. \end{aligned} \tag{1.22}$$

Thus, $\chi_{xxx}^{(2)}$ must vanish in order to satisfy $-P_x^{(2)} = P_x^{(2)}$ in general. Similarly, non-vanishing $\chi_{surface}^{(2)}$ tensor components can be determined. It turns out that $\chi_{surface}^{(2)}$ in silicon has five non-vanishing components and only three of them are independent. Taking into account the second order surface polarization equation (1.19) can be

written as [16]

$$\begin{pmatrix} P_x^{(2)} \\ P_y^{(2)} \\ P_z^{(2)} \end{pmatrix} = \begin{pmatrix} 0 & 0 & 0 & 0 & \chi_{xxz} & 0 \\ 0 & 0 & 0 & \chi_{yyz} & 0 & 0 \\ \chi_{zxx} & \chi_{zyy} & \chi_{zzz} & 0 & 0 & 0 \end{pmatrix} \begin{pmatrix} E_x E_x \\ E_y E_y \\ E_z E_z \\ 2E_y E_z \\ 2E_x E_z \\ 2E_x E_y \end{pmatrix}, \tag{1.23}$$

where $\chi_{xxz} = \chi_{yyz}$ and $\chi_{zxx} = \chi_{zyy}$. Equation (1.23) is also valid for isotropic materials such as amorphous SiO2 because they have the same surface symmetry properties as those of the silicon surface.

1.4 Theories of second harmonic generation in semiconductors

General theories of SHG have been developed by many groups over the last several decades. In 1962, N. Bloembergen and P. S. Pershan derived a general expression of SHG at the boundary of nonlinear media using Maxell's equations [17]. In 1983, H. Tom, T. Heinz and Y. Shen showed that silicon can contribute a bulk SHG response originating from the electric quadrupole moment of silicon [12]. The silicon bulk response showed rotational anisotropic SHG (RA-SHG) signals which reflected the crystal symmetry of silicon. An improved theory was introduced by Guyot-Sionnest et al. for the bulk contribution to the SHG signals [18]. A more general phenomenological development was achieved by Sipe et al. [16, 19]. In 2002, a simplified bond-hyperpolarizability model was developed by the Aspnes group [20] which was based on a polarizable bond model [21, 22]. This model could explain the RA-SHG signals in Si/SiO2 systems in detail. This model was further developed to calculate the third order susceptibility of silicon by the same group [23].

The nonlinear properties of GaAs crystal also have been studied. Unlike Si, GaAs has a non centro-symmetric crystal structure. Therefore it shows strong bulk SHG

responses which have a four-fold symmetric RA-SHG pattern. However the surface of GaAs has only two-fold symmetry. The interference of the two-fold and four-fold SHG signals in GaAs was reported by Yamada et al. [24]. Zinc-blende type crystals such as GaAs have only 6 non-vanishing bulk $\chi^{(2)}$ components and they are all identical. The nonlinear properties of $\chi^{(2)}$ of GaAs were studied phenomenologically by the same group [25] and also by Bergfeldet et al. [26].

1.5 Second harmonic generation experiments

Most nonlinear optical phenomena require intense light sources. Typically pulsed laser systems are used for nonlinear optical experiments. Many laser systems have the capability to generate intense pulsed beams on the order of GW/cm^2 peak intensity on sample surfaces. The Ti:Sapphire pulsed laser system is perhaps the most commonly used laser system for SHG experiments. This laser has a pulsed beam output with a tunable wavelength from 700 nm to 900 nm and pulse width of tens to hundreds of femtoseconds.

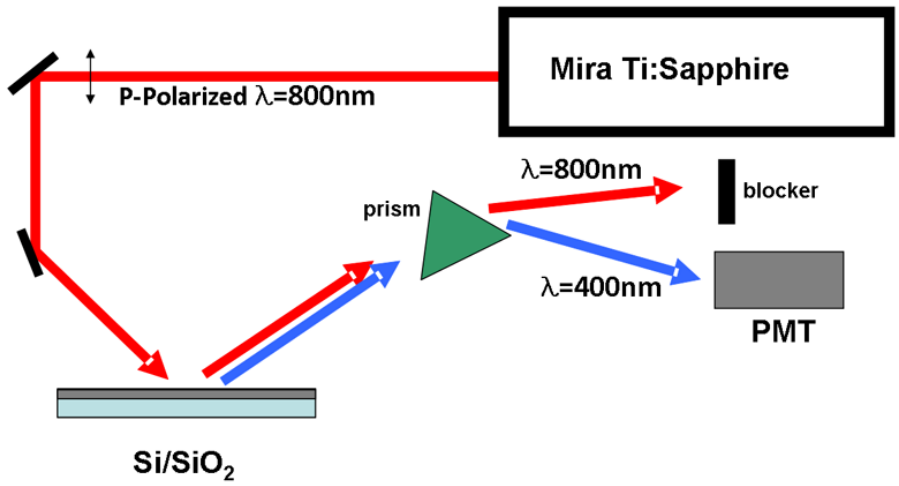

Figure 1.3: Schematic diagram of experimental setup for second harmonic generation.

In the experiments described in this thesis, P-polarized 800 nm fundamental light

is incident onto samples at 45°. SHG light (λ = 400 nm) is created in the samples and reflected. Reflected 800 nm and 400 nm beams are spatially separated by a prism. The 400 nm SHG beam is detected by a photo-multiplier-tube (PMT) which is sensitive to photons in the visible spectrum. The SHG intensity is measured by a photon counter. A Ti:Sapphire laser uses a mode-locking technique to create pulsed laser beams. A Mira Ti:Sapphire laser from Coherent Inc. has 76 MHz repetition rate which corresponds to a 13 ns pulse to pulse interval with a pulse width of 150 fs. A typical SHG experimental setup is shown in Fig. 1.3.

1.6 Quadratic dependence of second harmonic generation intensity

After setting up all experimental equipment, it needs to be tested to ensure that SHG signals are measured correctly. To do that, a power dependent SHG measurement can be performed. Because SHG intensity depends on the square of the fundamental beam intensity which is given by the equation (1.7), a quadratic dependence should be shown in the SHG measurement with respect to the fundamental beam intensity. A test sample needs to be chosen carefully. Depending on sample type, the magnitude of the SHG response is different. For example, non centro-symmetric materials such as GaAs and BBO(beta barium borate) crystal create very intense SHG signals. However centro-symmetric materials such as amorphous SiO2 and silicon create weak SHG signals. A thin oxide (thickness $<$ 10 nm) on silicon sample should be avoided for the test because it shows a slow time-dependent SHG response [5].

A thick oxide on silicon sample was tested for the quadratic dependence of the fundamental beam. The result is shown in Fig. 1.4. Its oxide thickness is 300 nm and the substrate is boron doped silicon(100). For the thick oxide on silicon wafer, the majority of SHG signals come from the interface $\chi^{(2)}$. The SHG intensities are fit by a quadratic equation of the fundamental beam intensity. The fit shows that the SHG intensity is proportional to $I(\omega)^{1.9}$ which is in a good approximation of the

quadratic dependence.

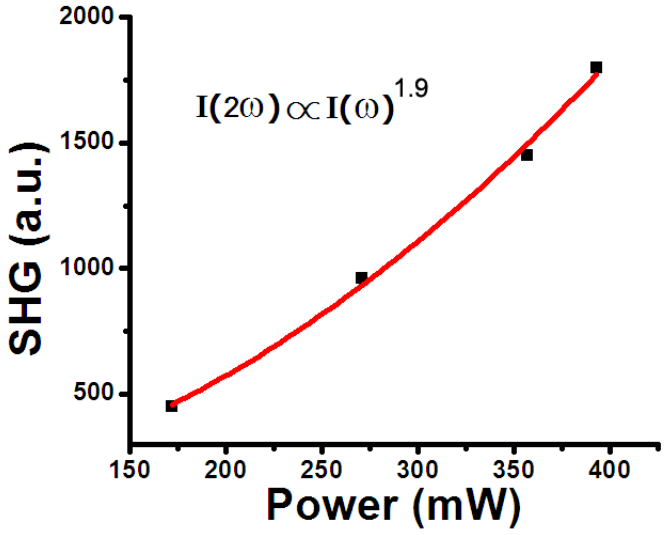

Figure 1.4: SHG intensities with respect to fundamental beam power. 300 nm thermal oxid on Si(100) wafer. The fit show approximate quadratic dependence.

CHAPTER II

ELECTRIC FIELD INDUCED SECOND HARMONIC GENERATION (EFISH)

Early work in DC electric field induced second harmonic generation (SHG) by a number of researchers is treated in this chapter. The first experimental result on electric field dependent SHG is identified. Electric field dependent SHG is showed to have a quadratic dependence in silicon. A quadratic dependence was also shown in a metal-oxide-semiconductor structure. Theoretical background is outlined relevant to electric field dependent SHG measurements. We also report on electron and hole dynamics as analyzed using time-dependent SHG measurements.

2.1 DC electric field induced second harmonic generation

The first DC electric field dependent SHG in silicon was reported by C. H. Lee et al. in 1967 [2]. They used a KCl solution to apply a DC electric field to p-type and n-type silicon samples. The SHG intensity was observed to have a quadratic dependence on the applied voltage. Figure 2.1 shows the experimental results. The SHG intensities are plotted with respect to the applied voltage in two different silicon samples (n-type and p-type wafers).

In 1996, another result on DC electric field dependent SHG was reported in a planar Cr-SiO2-Si MOS (metal-oxide-semiconductor) structure by O.A. Aktsipetrov et al. [3]. A DC electric field was applied by the capacitor-like structure and transmission SHG signals were monitored. Figure 2.2 shows the schematic diagram of the MOS structure. The experimental results also showed quadratic dependencies on the

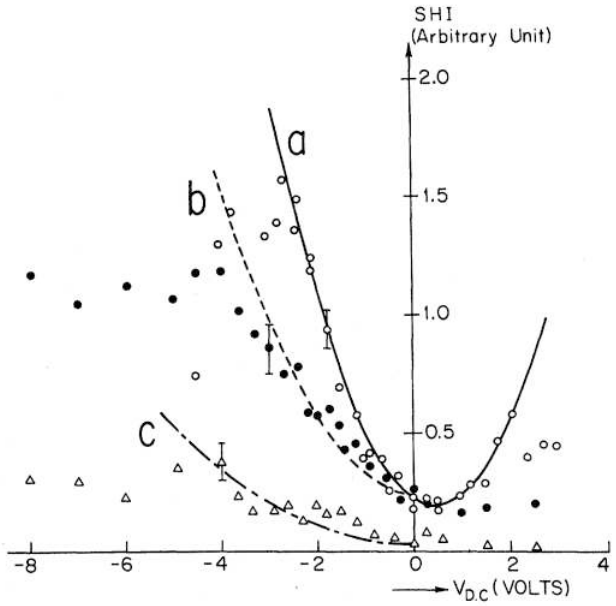

Figure 2.1: Applied voltage dependent SHG intensities from p-type (data a) and n-type(data b,c) silicon samples. Fundamental beam polarization direction is parallel to the incident plane for data a and b, and normal to the incident plane for data c [2].

applied DC electric field in the SHG signals, as shown in Fig. 2.3

The SHG signals were attributed mainly to three parts from the sample. The surface dipole contribution and the bulk electric quadrupole contribution from silicon are field independent. A DC electric field dependent contribution comes from the bulk silicon with broken symmetry by the DC electric field. However even though there is no applied external DC bias in the sample, a DC electric field exists near the interface of Si/SiO2, which is a space charge region (SCR). The DC electric field dependent contribution to the SHG signals is explained by the combination of the third order electric susceptibility $\chi^{(3)}$ and the external DC electric field E_{dc}. The main SHG contributions were written in two polarization equations. First, the silicon surface dipole and bulk quadrupole polarizations were given by [3]

$$P_{NL}(2\omega) = \chi^{(2),SD}(2\omega;\omega,\omega) : E(\omega)E(\omega) + \chi^{(2),BQ}(2\omega;\omega,\omega) : E(\omega)E(\omega)ik. \quad (2.1)$$

Second, the DC electric field dependent polarization was given as

$$P^{BD}(2\omega) = \chi^{(3)}(2\omega;\omega,\omega,0) : E(\omega)E(\omega)E_{dc}. \tag{2.2}$$

$\chi^{(2),SD}(2\omega;\omega,\omega)$ and $\chi^{(2),BQ}(2\omega;\omega,\omega)$ indicate the silicon surface dipole susceptibility and silicon bulk quadrupole susceptibility respectively. $\chi^{(3)}$ indicates the third order susceptibility of silicon. The quadratic dependence on the SHG with respect to the DC electric field is explained by the second order polarization equation which is given by

$$\begin{aligned} I(2\omega) &\propto P^{Total}(2\omega)^2 = (P_{NL} + P^{BD})^2 \\ &\propto {E_{dc}}^2. \end{aligned} \tag{2.3}$$

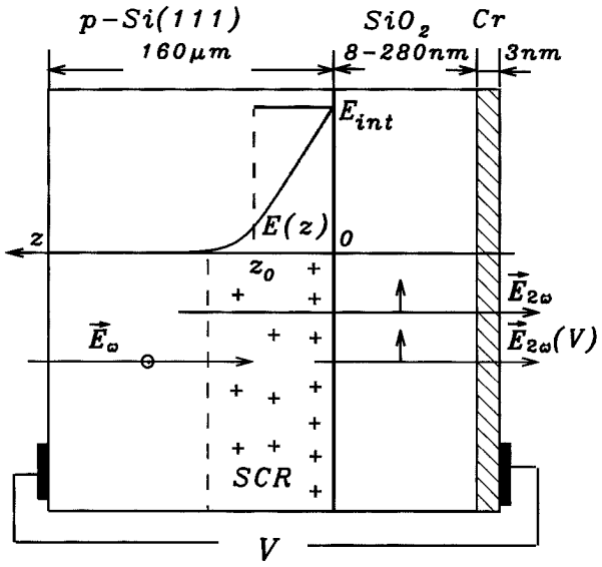

Figure 2.2: Schematic diagram of the MOS structure [3].

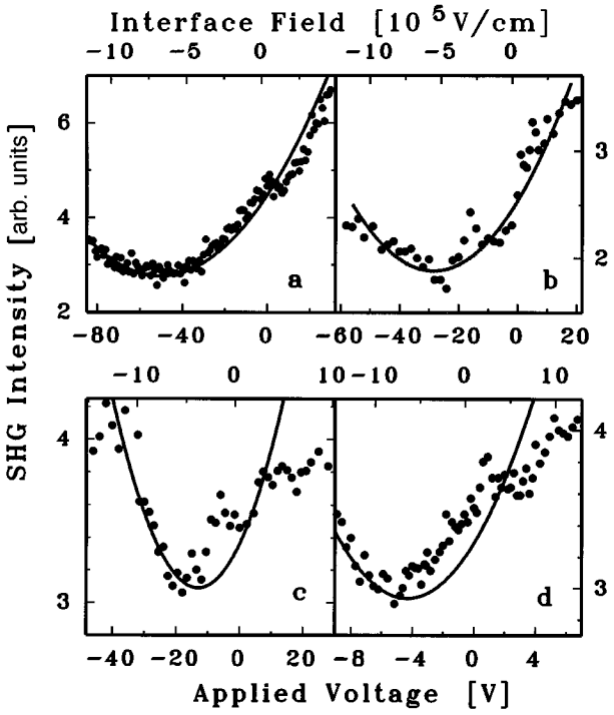

Figure 2.3: The SHG intensities vs an applied bias voltage V and an interface DC electric field for MOS samples with various oxide thickness: (a)234 nm, (b) 158 nm (c) 101 nm and (d) 18 nm. The solid lines are parabolic fitting curves [3].

2.2 $\chi^{(3)}$ contribution to SHG via E_{dc}

Nonlinear optical generation comes from the higher order polarizations given by the expansion of the polarization equation,

$$\begin{aligned} P &= \chi^{(1)}E + \chi^{(2)}E^2 + \chi^{(3)}E^3 + \cdots \\ &= P^{(1)} + P^{(2)} + P^{(3)} \cdots . \end{aligned} \tag{2.4}$$

The third-order susceptibility in equation (2.4), $\chi^{(3)}$, is responsible for third harmonic generation. However, when a DC electric field (E_{dc}) is present inside a material, SHG can also be induced from the third order susceptibility $\chi^{(3)}$. If E_{dc} is present in a material, the total electric field can be described by

$$E_{total}(t) = Ee^{-i\omega t} + Ee^{i\omega t} + E_{dc}. \tag{2.5}$$

From the power series expansion of the polarization equation (Eq. 2.4), the third order polarization equation, $P^{(3)} = \chi^{(3)} E^3_{total}$, contains 2ω terms due to the E_{dc} term. The doubled frequency electric field term $E(2\omega)$ can be written by

$$E(2\omega) \propto \chi^{(3)} E_{dc} E(2\omega)^2. \tag{2.6}$$

Therefore the SHG intensity with an E_{dc} term can be generally expressed by

$$I(2\omega) = \left|\chi^{(2)} + \chi^{(3)} E_{dc}\right|^2 I(\omega)^2. \tag{2.7}$$

In principle, the '=' sign should be replaced by '$\propto$'. However, the '=' sign is commonly used in experimental analysis. An exact relationship is given by equation (1.8). This DC electric field induced SHG is typically called EFISH.

Because SHG is sensitive to the DC electric field inside materials, SHG has been used as a powerful tool to study charge carrier dynamics in materials. In particular, for inversion symmetric materials such as silicon, the EFISH method becomes more useful in characterizing the surface or interface properties because the bulk contribution to SHG is much smaller than the surface and interface contributions [6, 27, 28].

2.3 Time-dependent SHG in Si/SiO2

In 1995 , a temporal behavior in SHG was reported in Si/SiO2 systems by Van. H. Driel group [4]. The SHG result showed a monotonic increase in time as shown in Fig. 2.4. The time-dependent SHG (TD-SHG) was attributed to a time-dependent DC electric field at the interface of Si/SiO2. The DC electric field was induced by a charge separation at the interface of Si/SiO2 by a multi-photon excitation process [5]. The charge separation was saturated after a long time which was shown by a saturated SHG level.

If the incoming photon energy is 1.55 eV (λ = 800 nm) and its intensity is low enough, the photon does not interact with the oxide because its bandgap is 9 eV. The photon interacts with silicon weakly since the silicon has 1.1 eV indirect bandgap.

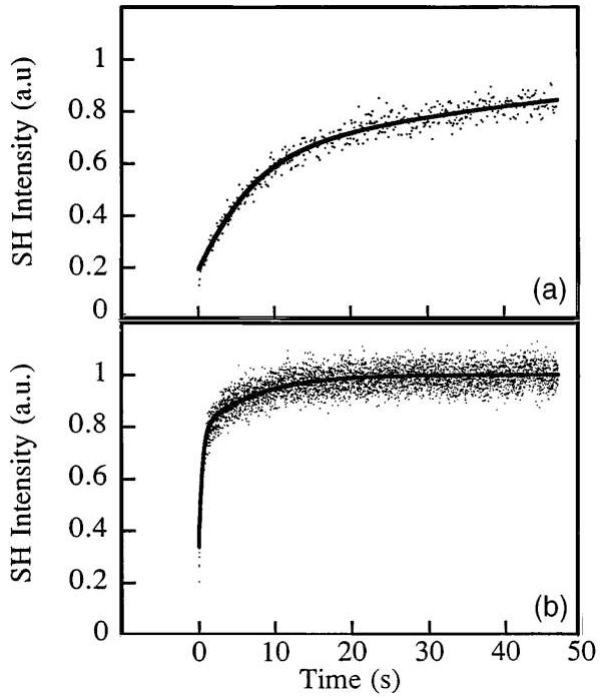

Figure 2.4: Time-dependent SHG signals in an oxidized Si(100) sample by a 770 nm beam for an incident irradiance of (a) 3 kW cm^2 and (b) 10 kW cm^2 [4].

Therefore at a sufficiently low intensity of the light, silicon absorbs the photons at a very low rate.

However, if the incoming light intensity is intense enough, the electrons at the silicon valence band can be excited by a three-photon excitation process. Because the band offset between the valence band of the silicon and the conduction band of the oxide is 4.5 eV, the three-photon absorption gives enough energy to an electron in the silicon valence band. After the three-photon excitation on the electron, it leaves a hole state in the valence band of silicon. The excited electron can travel through the oxide conduction band and arrive at the surface of the oxide. An oxygen molecule on the oxide surface can capture the electron. The remaining holes in the silicon valence band and the electrons captured by the oxygen molecules form a capacitor-like structure, which induces a DC electric field across the interface. A schematic

band diagram is shown in Fig. 2.5 regarding the three-photon excitation process in Si/SiO2 system.

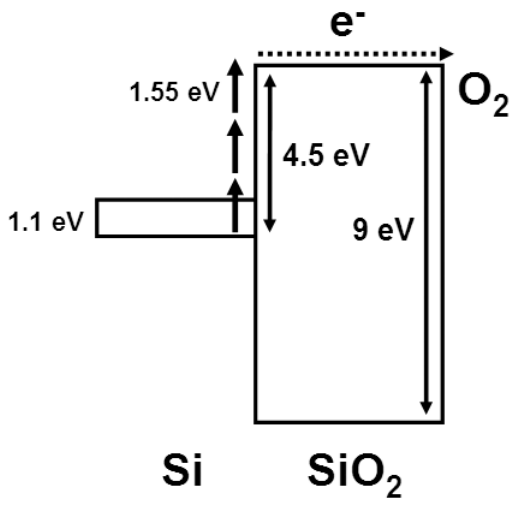

Figure 2.5: A schematic diagram of a three-photon electron excitation and transfer process of the electron.

The probability of a three-photon absorption process is very low, therefore the electron injection rate in filling the oxygen charge traps is also very low which results in a DC electric field that increases slowly. The slowly increasing E_{dc} can be detected by the EFISH measurement. J. Bloch, et al., showed that the saturated SHG level of Si/SiO2 depends on the thickness of the oxide [5]. As the oxide thickness increased, the saturated SHG level decreased. This oxide thickness effect comes from electron scattering during the electron traveling through the oxide. If the oxide was thicker than 10 nm, no time-dependent behavior was observed in the SHG measurements. In this case, all of the electrons come back to the silicon substrate after the scattering in the oxide. The oxide thickness dependent SHG experimental results are shown in Fig. 2.6 which plotted the saturated TD-SHG signals as a function of the oxide thickness from a p-type Si/SiO2 sample . As the oxide thickness increases, the saturated TD-

SHG level decreases. If the oxide thickness is greater than 10 nm, no time-dependent SHG signals are observed in the measurements.

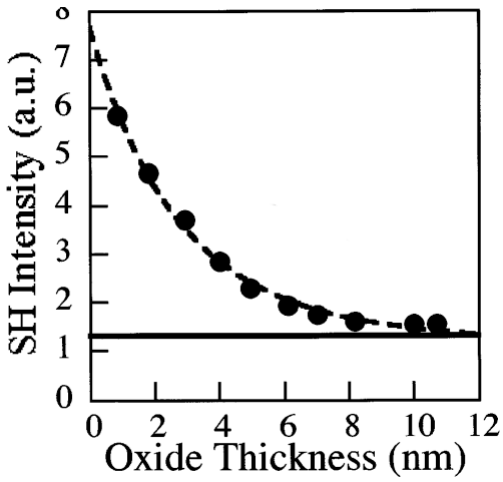

Figure 2.6: Oxide thickness dependent saturated SHG levels from p-Si(100) samples ; the horizontal solid line indicates the quiescent SHG level observed for all samples [5].

Because the interface DC electric field shows a time dependency, the DC electric field dependent SHG equation (2.7) can be expressed as

$$I(2\omega) = \left|\chi^{(2)} + \chi^{(3)} E_{dc}(t)\right|^2 I(\omega)^2. \tag{2.8}$$

This EFISH method has been extensively used to analyze material properties, especially in oxide on silicon systems. In particular, electron and hole dynamics were characterized in Si/SiO2 systems using the EFISH measurement [6, 29]. EFISH was used to study the interface charge trap properties in highly boron-doped Si/SiO2 [9, 10], Si/Al2O3 [30, 31], Si/HfO2 [30, 32], Si/MgO [33], Si/ZrO2 [30, 34], and SOI [35] systems. This method was also used to characterize the temperature dependent properties of the second and third order susceptibilities in Si/SiO2 [36] and the surface properties of chemically modified Si [37] and Ge [38] surfaces.

2.4 Electron and hole dynamics at the interface of Si/SiO2

Electron and hole dynamics were studied by time-dependent second harmonic generation (TD-SHG) measurements in Si/SiO2 systems [6]. Typically electrons can be injected by a multi-photon absorption process from the silicon valence band to the oxygen charge traps on the surface of the oxide. In addition to the electron injection, holes can be injected into the oxide from the silicon when the incoming fundamental laser beam is intense enough. The actual meaning of the hole injection to the oxide is electron transfer from the oxide to the silicon. The electrons in the valence band of the oxide may be excited by absorbing photons and transferring to the silicon conduction band leaving holes in the oxide valence band. The hole injection can occur by four-photon absorption at 800 nm wavelength ($h\nu = 1.55$ eV). Because a four-photon absorption has lower probability than three-photon absorption probability, it requires very intense light sources to inject the holes to the oxide.

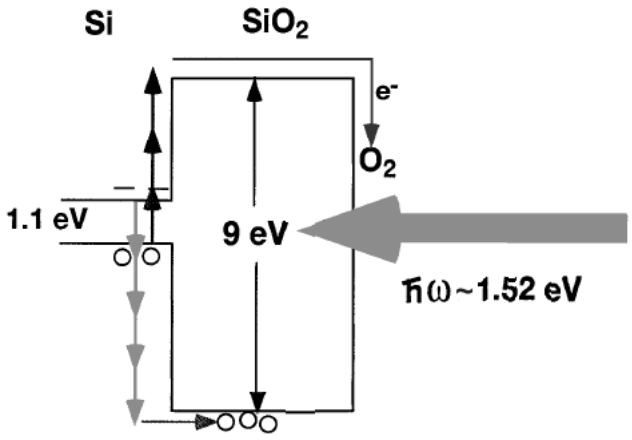

Figure 2.7: Schematic diagram of electron and hole injection dynamics in a thin oxide on silicon system [6].

A schematic diagram of the hole and electron injection is shown in Fig 2.7. Incoming photons may excite the electrons in the silicon valence band and in the oxide valence band by three photon absorption and four photon absorption, respectively.

The excited electrons create DC electric fields in opposite directions. Generally the interface electric field due to the oxygen charge traps saturates earlier than the interface electric field due to the hole injection. Therefore after saturating the oxygen charge traps, if holes are injected into the oxide (i.e. electrons are transfered from the oxide to the silicon leaving holes in the oxide), it reduces the magnitude of the total interface DC electric field. This hole injection effect is not easy to detect by a SHG measurement because electron detrapping from the oxygen traps makes the charge dynamics complicated. For thin oxide on silicon systems, electron injection, hole injection and electron detrapping occur simultaneously.

Electron detrapping from the oxygen molecular traps due to back tunneling may be negligible if the oxide thickness is about 4 nm. Even in this case, electrons and holes are injected into the oxide simultaneously at high laser beam intensity, but even when the laser is blocked, the oxide is thick enough to prevent the electron tunneling from the oxygen traps to the silicon. On the other hand the injected holes may be filled with the electrons in the silicon conduction band which were injected by the four-photon absorption process. The filled holes decrease the interface DC electric field which is induced by the hole injection. Thus total net DC electric field at the interface increases while the laser is blocked because the two interface electric fields are in opposite directions. The increased total interface DC electric field can be detected by a TD-SHG measurement.

The experimental results are shown in Fig 2.8. After the incoming beam was blocked for a while, the SHG measurement was resumed. It showed a significantly increased SHG signal (indicated by Δ_2) compared to the saturated SHG intensity (indicated by Δ_1). The SHG level was saturated by injecting electrons and holes in the oxide to the level of Δ_1. During the laser blocking, only the holes were filled by the electrons in the silicon conduction band, which resulted in an increasing total DC electric field at the interface. The increased total interface DC electric field was measured by resuming the SHG measurement, in which the SHG signal began at

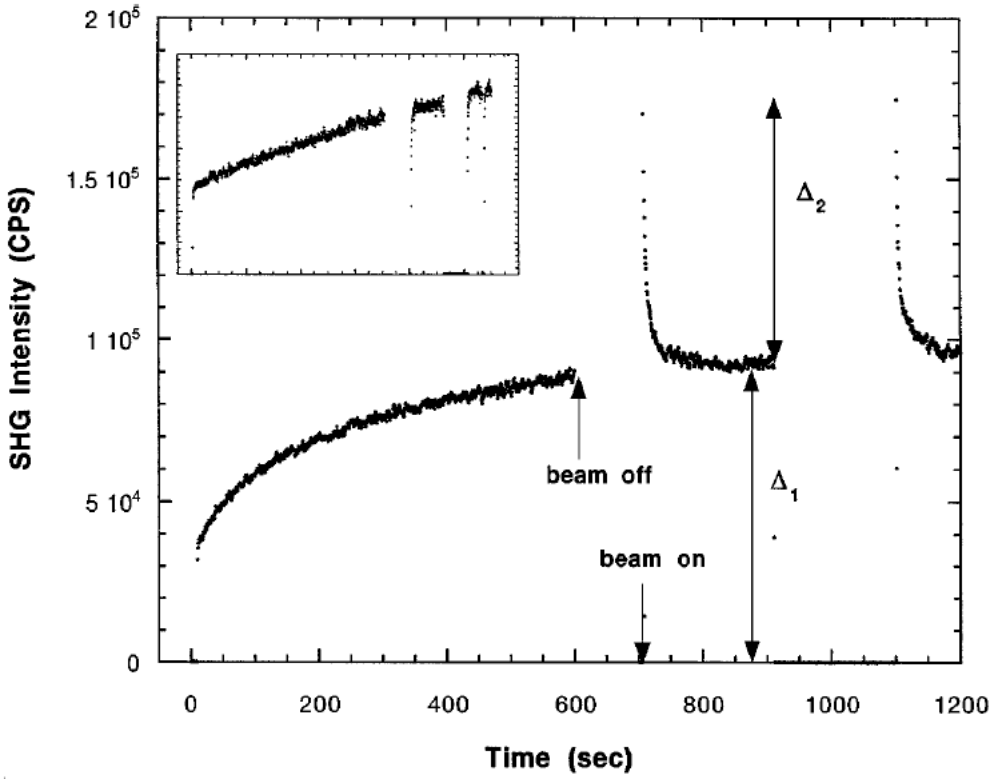

Figure 2.8: a TD-SHG signal from a 4 nm thick thermal oxide on a p-type silicon(100). Δ_1 represents a saturated SHG signal and Δ_2 represents the dark field enhanced SHG signal which is induced by hole (in the oxide) and electron (in the silicon) recombination. The inset shows the a TD-SHG signal from the same sample after the oxide has been etched. The oxide has a 1 nm thickness [6].

the level of Δ_2. The decreasing SHG signals after resuming the SHG measurements resulted from injecting holes again into the oxide.

CHAPTER III

POLARIZATION-DEPENDENT SECOND HARMONIC GENERATION IN Si/SiO2

This chapter describes both experimental results and theoretical work on the polarization-dependent temporal behavior of second harmonic generation in thin oxide on silicon(100) systems. It is shown that the experimental results can be explained mainly by the dipole radiation approximation. We observed a critical incident polarization angle between P_{in} and S_{in} fundamental beams, in which no temporal variation exist in the P_{out} SHG signal [39]. We also observed that the critical angle is independent of dopant type, concentration, oxide thickness and oxide type. A quadrupole radiation contribution to the second harmonic generation signals is also included at the end of the chapter.

3.1 Introduction

Second harmonic generation (SHG) is a powerful tool for the study of material surfaces and buried interfaces. It is well known that intense laser radiation induced SHG vanishes under the dipole radiation approximation for inversion symmetric materials such as silicon [16, 40, 41]. Therefore, for such materials, surface and interface contributions are the major sources of SHG. When an electric field is present at the interface of Si/SiO2, SHG is enhanced by a fourth rank tensor contribution, $\chi^{(3)}E_{dc}$ [3, 27, 28, 42, 43], which is called electric-field-induced SHG (EFISH).

EFISH has been utilized to study the interfaces of many semiconductor-oxide materials. In previous research, electron and hole dynamics were analyzed in Si/SiO2

systems using the EFISH approach [6, 29] EFISH was also used to study the interface properties in highly boron-doped Si/SiO2 [9, 10], Si/Al2O3 [30, 31], Si/HfO2 [30, 32], Si/MgO [33], Si/ZrO2 [30, 34], and SOI [35] systems. In these systems a quasi-static electric field is created arising from the separation of charge carriers.

If the oxide is thin (less than 10nm) in Si/SiO2, a time-dependent SHG (TD-SHG) measurement shows a monotonic increase [4, 5]. To characterize the TD-SHG signal, the following equation has been used [5, 6].

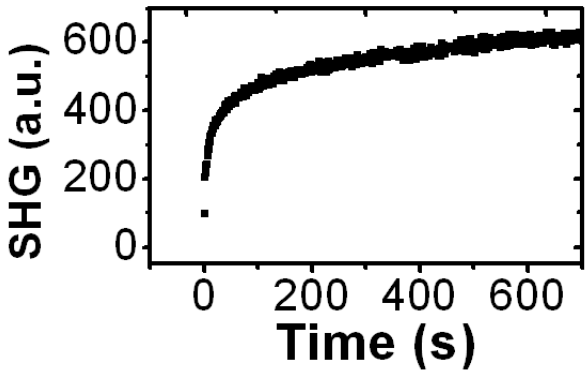

Figure 3.1: TD-SHG measurement in Sb doped Si/SiO2. The oxide thickness is about 2 nm. Resistivity: 0.001-0.02 Ωcm.

$$I(2\omega) = \left|\chi^{(2)} + \chi^{(3)} E_{dc}(t)\right|^2 I(\omega)^2, \tag{3.1}$$

where $\chi^{(2)}$ and $\chi^{(3)}$ are the effective non-linear second- and third-order electric susceptibilities near the Si/SiO2 interface, respectively. $E_{dc}(t)$ is a time-dependent DC electric field across the interface. For accurate description, the " = " sign should be replaced by the proportional symbol " $\propto$ ". However (3.1) is commonly used in experimental analysis.

If thin oxide on silicon systems are irradiated with 800 nm wavelength light ($h\nu$ = 1.55 eV), electrons in the silicon valence band can be exited by a three-photon absorption process above the conduction band of the oxide [6, 44]. These electrons

can travel across the oxide to reach the surface. They leave the remaining holes near the interface. Finally the electrons may be captured by the ambient oxygen molecules on the surface of the oxide, resulting in the creation of a DC electric field across the Si/SiO2 interface due to the electron-hole pair separation. The increase of the DC electric field can be detected by a SHG measurement. A typical TD-SHG result is shown in Fig 3.1 indicating a monotonic increase in time due to the increase of the interface DC electric field.

3.2 Experimental setup for polarization-dependent second harmonic generation

Because SHG involves two-photon absorption, it requires intense light sources to generate SHG light. Typically pulsed laser systems are used in SHG experiments in which their peak beam intensity is on the order of GW/cm^2 on sample surfaces. A Mira Ti:Sapphire laser was used in polarization-dependent SHG experiment. The laser has a repetition rate of 75 MHz and a pulse width of about 150 fs. A variable linearly polarized 800 nm beam was directed onto the samples at 45° using a half wave ($\lambda/2$) plate. By rotating the wave plate in 180°, the linearly polarized fundamental beam is rotated continuously from 0° to 360°. Upon reflection, a prism separated the fundamental beam ($\lambda = 800\,nm$) and doubled frequency beam ($\lambda = 400\,nm$). The 400 nm SHG beam was detected using a photo-multiplier-tube (PMT) and a photon counter. Samples were aligned such that the (100) crystal orientation was parallel to the incident beam plane and rotated about the sample normal to measure the azimuthal angle dependent SHG signals. The typical experimental setup is shown in Fig. 3.2.

Because a prism has polarization-dependent transmissions, the effect should be accounted in analyzing the SHG intensities of P- and S-polarized beams. To avoid this complexity, a band-pass filter can be used to filter out the 800 nm fundamental beam.

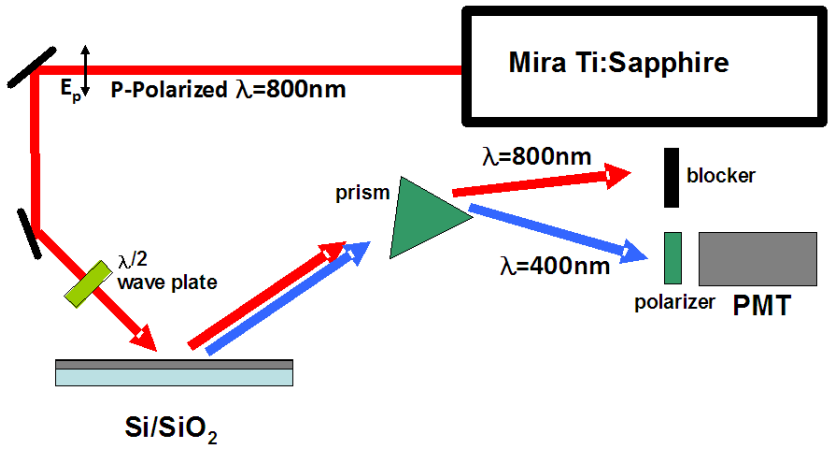

Figure 3.2: Schematic of polarization-dependent SHG experimental setup.

However, in addition to the prism effect, mirrors also have polarization-dependent reflectance. For accurate measurement all of the polarization dependent effects must be accounted. Various silicon(100) wafers were used in the polarization dependent SHG experiments. Wafer descriptions are shown in Table 3.1. The oxide thicknesses were measured by ellipsometry.

3.3 Polarization-dependent TD-SHG measurements in thin oxides on silicon (100) substrates

TD-SHG responses in the Si(100)/SiO2 systems are highly dependent on the polarization direction of the fundamental beam. Experimental results are shown in Fig. 3.3. Strong time-dependencies are observed in P-polarized SHG measurements for P- and S-polarized fundamental beams ($P_{in} - P_{out}$ and $S_{in} - P_{out}$ respectively). For the S-polarized SHG measurements, however, no time-dependencies are observed from both fundamental polarizations ($P_{in} - S_{out}$ and $S_{in} - S_{out}$). The same results are also obtained from all the samples in Table 3.1.

Equation (3.1) is typically used to characterize TD-SHG signals in thin oxide Si/SiO2 systems. However the exact tensor form of equation (3.1) should be known to

Table 3.1: Descriptions of silicon(100) samples.

Wafer label	Dopant	Resistivity (Ωcm)	Oxide type	Oxide thickness (nm)
Wafer 1	Boron	5-15	Native SiO_2	2.45
Wafer 2	Boron	0.01-0.02	Native SiO_2	2.40
Wafer 3	Boron	0.001-0.009	Native SiO_2	2.64
Wafer 4	Boron	0.001-0.009	Thermal SiO_2	4.94
Wafer 5	Phosphorus	1-100	Native SiO_2	2.09
Wafer 6	Arsenic	0.001-0.005	Native SiO_2	2.12
Wafer 7	Arsenic	0.001-0.005	Thermal SiO_2	5.97
Wafer 8	Antimony	0.001-0.025	Native SiO_2	2.39
Wafer 9	Unknown (n-type)	1-10	Native SiO_2	4.23

explain the polarization dependencies in the TD-SHG results. Based on a dimensional analysis, $\chi^{(2)}$ and $\chi^{(3)}E(t)$ should have the same dimension as rank three tensors. Therefore the product $\chi^{(3)}E(t)$ produces a rank three tensor from the rank four $\chi^{(3)}$ tensor by tensor contraction. Because $\chi^{(3)}$ has generally 81 components with 18 non-vanishing components, in which three of them are independent in bulk silicon [30,42], it seems a tedious job to calculate $\chi^{(3)}E(t)$ by tensor algebra. But a simple tensor form of the equation can be obtained only using a symmetry analysis when E(t) is directed along the sample normal (z-axis). This symmetry analysis was briefly discussed by Heinz without elaboration [45]. The tensor formulation is explained in great detail in this section.

In Fig. 3.4, the fundamental electric field is expressed in the sample coordinate system with the x-axis along the (100) crystal plane and y-axis along the (010) crystal plane. We consider only the dipole radiation approximation to expain the TD-SHG results. Weak bulk signals from magnetic dipoles and electric quadrupoles may contribute [16], but their magnitudes are much smaller than the dipole SHG contribution.

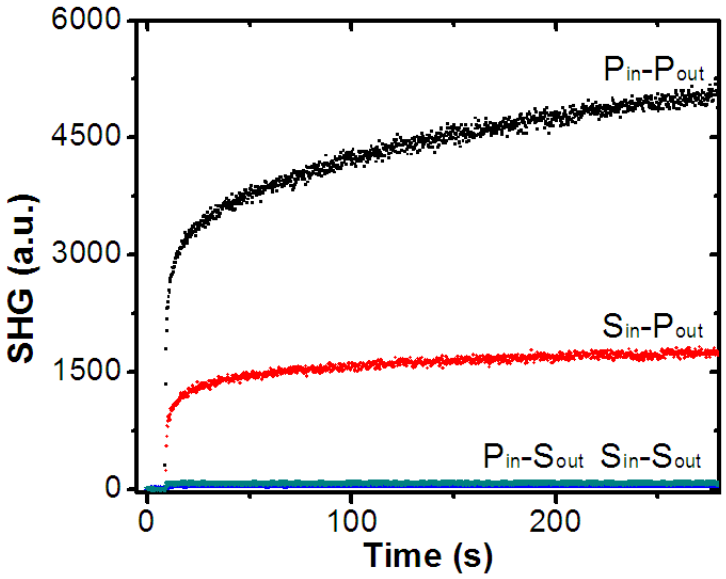

Figure 3.3: TD-SHG experimental results in four different polarization configurations. The sample is a boron-doped Si(100) wafer with a native oxide and with a resistivity of 5-15 Ωcm. The incident plane is parallel to (100) crystal plane. Initially, the laser beam was blocked for the first 10 s.

The higher order nonlinear polarization contributions are discussed at the end of this chapter.

In bulk silicon, a DC electric field, $E_{dc}(t)$, breaks the inversion symmetry of Si crystal. If $E_{dc}(t)$ is directed along the z axis, the bulk symmetry has the same properties as the symmetry in silicon (100) surface. Therefore we may consider an electric-field-dependent effective third rank tensor $\chi^{(2)}(E_{dc})$ which governs SHG responses from the silicon (100)/oxide interface. Thus, the following equation can be used to characterize the experimental results,

$$I(2\omega) = \left|\chi^{(2)}(E_{dc})\right|^2 I(\omega)^2. \tag{3.2}$$

Because of the mirror symmetry in the x and y axes near the interface of silicon and oxide in which there is an induced interface DC electric field E_{dc}, the second order polarization may be expressed in the form [16] of

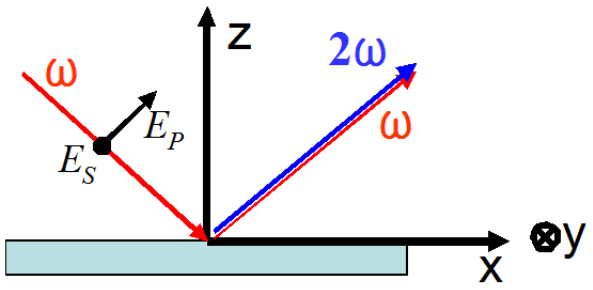

Figure 3.4: Schematic diagram of the sample and beam polarization configuration.

$$\begin{pmatrix} P_x^{(2\omega)} \\ P_y^{(2\omega)} \\ P_z^{(2\omega)} \end{pmatrix} = \begin{pmatrix} 0 & 0 & 0 & 0 & \chi_{xxz}(E_{dc}) & 0 \\ 0 & 0 & 0 & \chi_{yyz}(E_{dc}) & 0 & 0 \\ \chi_{zxx}(E_{dc}) & \chi_{zyy}(E_{dc}) & \chi_{zzz}(E_{dc}) & 0 & 0 & 0 \end{pmatrix} \begin{pmatrix} E_x E_x \\ E_y E_y \\ E_z E_z \\ 2E_y E_z \\ 2E_x E_z \\ 2E_x E_y \end{pmatrix} \tag{3.3}$$

, with three independent components: $\chi_{xxz} = \chi_{yyz}$, $\chi_{zxx} = \chi_{zyy}$, χ_{zzz}. Thus it can be written in a simpler form,

$$\begin{pmatrix} P_x^{(2\omega)} \\ P_y^{(2\omega)} \\ P_z^{(2\omega)} \end{pmatrix} =$$

$$\begin{pmatrix} 0 & 0 & 0 & 0 & \chi_{xxz}(E_{dc}) & 0 \\ 0 & 0 & 0 & \chi_{xxz}(E_{dc}) & 0 & 0 \\ \chi_{zxx}(E_{dc}) & \chi_{zxx}(E_{dc}) & \chi_{zzz}(E_{dc}) & 0 & 0 & 0 \end{pmatrix} \begin{pmatrix} E_xE_x \\ E_yE_y \\ E_zE_z \\ 2E_yE_z \\ 2E_xE_z \\ 2E_xE_y \end{pmatrix}. \tag{3.4}$$

Each component is expanded with respect to the DC electric field (E_{dc}). Under the small perturbation approximation (We assume that the interface DC electric field E_{dc} is small), it can be expressed as

$$\begin{pmatrix} P_x^{(2\omega)} \\ P_y^{(2\omega)} \\ P_z^{(2\omega)} \end{pmatrix} =$$

$$\begin{pmatrix} 0 & 0 & 0 & 0 & \chi^0_{xxz} + \chi^1_{xxz}E_{dc} & 0 \\ 0 & 0 & 0 & \chi^0_{xxz} + \chi^1_{xxz}E_{dc} & 0 & 0 \\ \chi^0_{zxx} + \chi^1_{zxx}E_{dc} & \chi^0_{zxx} + \chi^1_{zxx}E_{dc} & \chi^0_{zzz} + \chi^1_{zzz}E_{dc} & 0 & 0 & 0 \end{pmatrix}$$

$$\begin{pmatrix} E_xE_x \\ E_yE_y \\ E_zE_z \\ 2E_yE_z \\ 2E_xE_z \\ 2E_xE_y \end{pmatrix}. \tag{3.5}$$

This equation is equivalent to equation (3.1) and shows that the tensor $\chi^{(2)}(E_{dc})$ includes also field-independent terms, $(\chi^0_{xxz}, \chi^0_{zxx}, \chi^0_{zzz})$. The difference in form comes

from underlying assumptions in each equation. Equation (3.1) assumes that E_{dc} is small enough not to change $\chi^{(2)}$ and $\chi^{(3)}$. Equation (3.5) assumes that $\chi^{(2)}$ is changed as a function of E_{dc}. Only the first two terms are used in the expansion under the small E_{dc} approximation and the higher order terms of E_{dc} are negligible.

As long as the tensor components are defined, it is straightforward to obtain a polarization-dependent SHG response from the equation. A similar result was shown in research involving isotropic materials which have the same mirror symmetry through x- and y-axes on the surface of the materials [45]. Equation (3.5) may be simplified to the following expression

$$\begin{pmatrix} P_x^{(2\omega)} \\ P_y^{(2\omega)} \\ P_z^{(2\omega)} \end{pmatrix} = \begin{pmatrix} (\chi^0_{xxz} + \chi^1_{xxz} E_{dc}) 2E_x E_z \\ (\chi^0_{xxz} + \chi^1_{xxz} E_{dc}) 2E_y E_z \\ (\chi^0_{zxx} + \chi^1_{zxx} E_{dc}) E_x^2 + (\chi^0_{zxx} + \chi^1_{zxx} E_{dc}) E_y^2 + (\chi^0_{zzz} + \chi^1_{zzz} E_{dc}) E_z^2 \end{pmatrix}. \quad (3.6)$$

For a P-polarized fundamental beam Ey = 0, but Ex and Ez are not zero. Equation (3.6) becomes

$$\begin{pmatrix} P_x^{(2\omega)} \\ P_y^{(2\omega)} \\ P_z^{(2\omega)} \end{pmatrix} = \begin{pmatrix} (\chi^0_{xxz} + \chi^1_{xxz} E_{dc}) 2E_x E_z \\ 0 \\ (\chi^0_{zxx} + \chi^1_{zxx} E_{dc}) E_x^2 + (\chi^0_{zzz} + \chi^1_{zzz} E_{dc}) E_z^2 \end{pmatrix}. \quad (3.7)$$

The incident beam polarization-dependent SHG responses (P-polarized SHG: and S-polarized SHG:) between SiO2 which is a linear medium 1, and Si which is a nonlinear medium 2, can be written as follows [12, 13]

$$\begin{aligned} E_P^{(2\omega)} &= \frac{i4\pi k_1}{\epsilon_2 k_{1z} + \epsilon_1 k_{2z}} (k_{2z} P_x^{(2\omega)} + k_{2x} P_z^{(2\omega)}) \\ &= A_x P_x^{(2\omega)} + A_z P_z^{(2\omega)}, \end{aligned} \quad (3.8)$$

$$\begin{aligned} E_S^{(2\omega)} &= \frac{i4\pi k_1}{k_{1z} + k_{2z}} \frac{k_1}{\epsilon_1} P_y^{(2\omega)} \\ &= A_y P_y^{(2\omega)}, \end{aligned} \quad (3.9)$$

where the proportionality coefficients Ax, Ay and Az are used to simplify the expressions, and k_i and ϵ_i are wave vectors and dielectric constants at 2ω in medium 1 and

2 respectively. Thus the SHG responses for the P-polarized fundamental beams are

$$\begin{aligned} E^{(2\omega)}_{P\to P} &= A_x P^{(2\omega)}_x + A_z P^{(2\omega)}_z \\ &= B_1 + B_2 E_{dc}(t), \end{aligned} \tag{3.10}$$

$$\begin{aligned} E^{(2\omega)}_{P\to S} &= \frac{i4\pi k_1}{k_{1z}+k_{2z}} \frac{k_1}{\epsilon_1} P^{(2\omega)}_y \\ &= A_y P^{(2\omega)}_y, \end{aligned} \tag{3.11}$$

where the B_i are proportionality coefficients which arise from the wave vectors, dielectric constants, fundamental electric field $E^{(\omega)}$, and electric susceptibilities in equations (3.7-3.10). This analysis shows a strong time-dependency in P-polarized TD-SHG and no time-dependency in S-polarized TD-SHG. In fact, the S-polarized TD-SHG actually vanishes in the dipole radiation approximation. For an S-polarized fundamental beam Ex and Ez are zero, but Ey is not zero. Thus, equation (3.6) becomes

$$\begin{pmatrix} P^{(2)}_x \\ P^{(2)}_y \\ P^{(2)}_z \end{pmatrix} = \begin{pmatrix} 0 \\ 0 \\ (\chi^0_{zxx} + \chi^1_{zxx} E_{dc}) E^2_y \end{pmatrix}, \tag{3.12}$$

and

$$\begin{aligned} E^{(2\omega)}_{S\to P} &= A_z P^{(2\omega)}_z \\ &= B_3 + B_4 E_{dc}(t), \end{aligned} \tag{3.13}$$

$$\begin{aligned} E^{(2\omega)}_{S\to S} &= A_x P^{(2\omega)}_x \\ &= 0. \end{aligned} \tag{3.14}$$

A time-dependency is predicted for P-polarized SHG and no time-dependency for S-polarized SHG. However there are non-zero weak S-polarized SHG signals in Fig. 3.3. The weak SHG signals come from higher order non-linear terms such as electric quadrupole and magnetic dipole moment contributions. This simple explanation accounts for the experimental results shown in Fig. 3.3. This description is consistent with previous research of Fomenko et al., in which the $\chi^{(2)}$ contribution is ignored [30]. Equations (3.10, 3.11, 3.13) can be used to find relationships of $\chi^{(1)}_{ijk}$ and $\chi^{(3)}$ with an

arbitrary incident angle θ. From those, we can obtain the field dependent components $\chi^{(1)}_{xxz}$, $\chi^{(1)}_{zxx}$, $\chi^{(1)}_{zzz}$ in terms of the rank four $\chi^{(3)}$ tensor components of Eq. (3.1) by comparing Eq. (3) and Eq. (4) in ref. [30]. The three independent components $(\chi^{(3)}_1, \chi^{(3)}_2, \chi^{(3)}_3)$ of $\chi^{(3)}$ are defined as

$$\begin{aligned}
\chi^{(3)}_1 &= \chi_{xxxx} = \chi_{yyyy} = \chi_{zzzz}, \\
\chi^{(3)}_2 &= \chi_{xyyz} = \chi_{yxxy} = \chi_{xzzx} = \chi_{yzzy} = \chi_{zxxz} = \chi_{zyyz}, \\
\chi^{(3)}_3 &= \chi_{xyxy} = \chi_{xxyy} = \chi_{yyxx} = \chi_{yxyx} = \chi_{xyyx} = \chi_{xxzz} = \chi_{xzxz} \\
&= \chi_{yyzz} = \chi_{yzyz}.
\end{aligned} \tag{3.15}$$

Thus, we have determined $\chi^1_{xxz} = \chi^{(3)}_3, \chi^1_{zxx} = \chi^{(3)}_2, \chi^1_{zzz} = \chi^{(3)}_1$, and therefore we have a completely defined tensor expression of equation (3.1) as

$$\begin{pmatrix} P^{(2)}_x \\ P^{(2)}_y \\ P^{(2)}_z \end{pmatrix} =$$

$$\begin{pmatrix}
0 & 0 & 0 & 0 & \chi^{(2)}_{xxz} + \chi^{(3)}_3 E_{dc} & 0 \\
0 & 0 & 0 & \chi^{(2)}_{xxz} + \chi^{(3)}_3 E_{dc} & 0 & 0 \\
\chi^{(2)}_{zxx} + \chi^{(3)}_2 E_{dc} & \chi^{(2)}_{zxx} + \chi^{(3)}_2 E_{dc} & \chi^{(2)}_{zzz} + \chi^{(3)}_1 E_{dc} & 0 & 0 & 0
\end{pmatrix}$$

$$\begin{pmatrix} E_x E_x \\ E_y E_y \\ E_z E_z \\ 2E_y E_z \\ 2E_x E_z \\ 2E_x E_y \end{pmatrix}. \tag{3.16}$$

Note, there is a typographical error in ref. [30]. In equation (3) and (4) in the reference, $\chi^{(3)}_2$ and $\chi^{(3)}_3$ should be exchanged.

3.4 Critical polarization angle

The angle φ is defined as the polarization angle measured from the P-polarized fundamental beam orientation. $\varphi = 0$ corresponds to P polarization, and $\varphi = 90°$ corresponds to S polarization. If the incident angle is at 45°, the electric field components of the fundamental beam are

$$\begin{pmatrix} E_x \\ E_y \\ E_z \end{pmatrix} = \begin{pmatrix} \frac{1}{\sqrt{2}} E cos\varphi \\ E sin\varphi \\ \frac{1}{\sqrt{2}} E cos\varphi \end{pmatrix}, \tag{3.17}$$

where E is the amplitude of the fundamental beam. Therefore equation (3.6) becomes

$$\begin{pmatrix} P_x^{(2)} \\ P_y^{(2)} \\ P_z^{(2)} \end{pmatrix} = \begin{pmatrix} (\chi^0_{xxz} + \chi^1_{xxz} E_{dc}) cos^2\varphi E^2 \\ (\chi^0_{xxz} + \chi^1_{xxz} E_{dc}) \sqrt{2} sin\varphi cos\varphi E^2 \\ (\chi^0_{zxx} + \chi^1_{zxx} E_{dc})(sin^2\varphi + \frac{1}{2} cos^2\varphi) E^2 + (\chi^0_{zzz} + \chi^1_{zzz} E_{dc}) \frac{1}{2} cos^2\varphi E^2 \end{pmatrix}, \tag{3.18}$$

and the SHG signals become functions of the polarization angle φ and the other tensor components. $E^{(2\omega)}_{\varphi \to P} = A_x P_x^{(2\omega)} + A_z P_z^{(2\omega)}$ can be expressed in simple terms to be

$$E^{(2\omega)}_{\varphi \to P} = \alpha(E_{dc}) cos^2\varphi + \beta(E_{dc}) sin^2\varphi, \tag{3.19}$$

where α, β are the DC field-dependent terms defined by

$$\alpha(E_{dc}) = A_x(\chi^0_{xxz} + \chi^1_{xxz} E_{dc}) E^2 + \frac{1}{2} A_z(\chi^0_{zxx} + \chi^1_{zxx} E_{dc}) E^2 + \frac{1}{2} A_z(\chi^0_{zzz} + \chi^1_{zzz} E_{dc}) E^2,$$

$$\beta(E_{dc}) = A_z(\chi^0_{zxx} + \chi^1_{zxx} E_{dc}) E^2.$$

The corresponding SHG intensity is

$$\begin{aligned} I^{(2\omega)}_{\varphi \to P} &= |E^{(2\omega)}_{\varphi \to P}|^2 \\ &= |\alpha(E_{dc}) cos^2\varphi + \beta(E_{dc}) sin^2\varphi|^2. \end{aligned} \tag{3.20}$$

By the same way, the S-polarized SHG expressions may be written

$$\begin{aligned} E^{(2\omega)}_{\varphi\to S} &= A_y P^{(2\omega)}_y \\ &= A_y(\chi^0_{xxz} + \chi^1_{xxz}E_{dc})\sqrt{2}E^2 sin\varphi cos\varphi, \end{aligned} \tag{3.21}$$

$$\begin{aligned} I^{(2\omega)}_{\varphi\to S} &= |E^{(2\omega)}_{\varphi\to S}|^2 \\ &= |A_y(\chi^0_{xxz} + \chi^1_{xxz}E_{dc})\sqrt{2}E^2|^2 (sin\varphi cos\varphi)^2. \end{aligned} \tag{3.22}$$

The S-polarized TD-SHG signal is maximized at $\varphi = 45°$, and becomes zero both at $0°(P_{in})$ and at $90°(S_{in})$. Experimental results as shown in Fig. 3.5 are consistent with the predictions of equation (3.22). From equation (3.22), it is clear that the tensor component χ_{xxz} can be effectively determined by taking a $45°_{in} - S_{out}$ measurement if E_{dc} is known. χ_{zxx} can be experimentally determined using (3.13). Following these, χ_{zzz} also can be determined using (3.10). Therefore in principle all tensor components can be acquired from the polarization-dependent TD-SHG measurements.

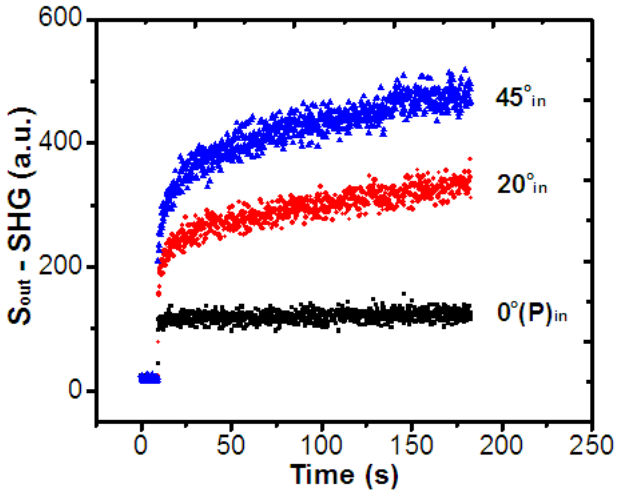

Figure 3.5: Incident polarization angle dependent S-polarized TD-SHG signals. The incident plane is parallel to (100) crystal plane. Initially, the laser beam was blocked for the first 10 s.

In each sample used in these measurements, a particular critical incident po-

larization angle could be found in which no time-dependency in P-polarized SHG measurements was observed. It was observed that the critical angle is independent of oxide type, thickness, dopant type, and dopant concentration. All silicon (100) wafer samples described in Table 3.1 showed the characteristic non-time-independent behavior at 57° polarization angle for P-polarized SHG. One TD-SHG result is shown in Fig. 3.6.(a)-($57^{\circ}_{in} - P_{out}$). It was confirmed that though there is no time-dependent increase in the P-polarized SHG at the critical incident angle, during the irradiation electron-hole pairs are created and charges are spatially separated. Finally a DC electric field is formed. To show this, in Fig. 3.6.(a), the incident polarization angle was initially set at $\varphi = 57^{\circ}$ (the critical angle) and then changed quickly to $\varphi = 0^{\circ}(P_{in})$ at 185 s. After changing the incident polarization from 57°_{in} to P_{in}, the SHG intensity showed a highly saturated level as shown in Fig. 3.6.(a)-($P_{in} - P_{out}$) indicating the presence of a significant DC electric field at the interface. The signal can be compared to the $P_{in} - P_{out}$ SHG signal (Fig. 3.6.(b)) measured from a fresh location of the sample. The slight discrepancy between the measured saturation levels shown in Fig. 3.6 most probably comes from a non-uniform sample surface and an incident polarization-dependent electron injection rate.

To explain the non-temporal behavior in the P-polarized SHG signal, we can express equation (3.19) as

$$E^{(2\omega)}_{\varphi \to P} = \gamma + \delta E_{dc}(t), \tag{3.23}$$

where γ and δ are defined as

$$\gamma = [(A_x \chi^0_{xxz} + \frac{1}{2} A_z \chi^0_{zxx} + \frac{1}{2} A_z \chi^0_{zzz}) cos^2\varphi + A_z \chi^0_{zxx} sin^2\varphi] E^2,$$

$$\delta = [(A_x \chi^1_{xxz} + \frac{1}{2} A_z \chi^1_{zxx} + \frac{1}{2} A_z \chi^1_{zzz}) cos^2\varphi + A_z \chi^1_{zxx} sin^2\varphi] E^2.$$

At the critical angle, δ is shown to vanish. In this case, the P-polarized SHG arises entirely from the field-independent γ and higher order non-linear polarizations. As discussed, the critical angle is determined only by the substrate properties, as expressed in the χ^1_{ijk} terms in equation (3.5) (equivalently from equation (3.15)) .

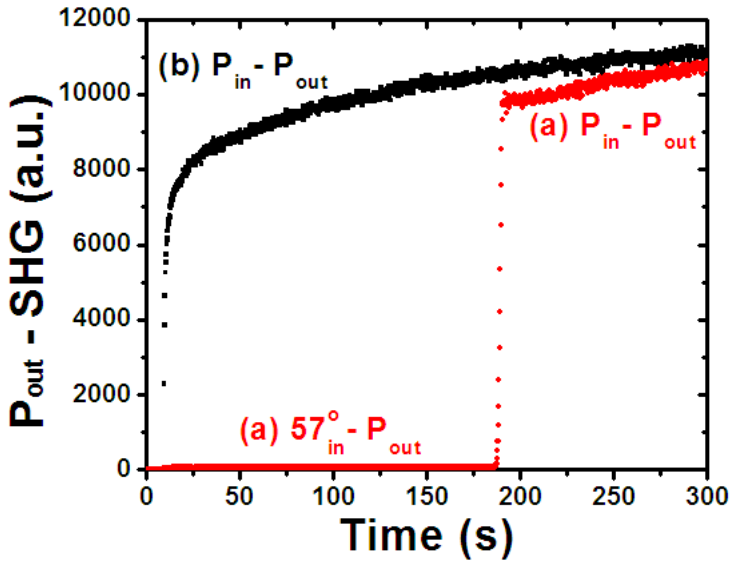

Figure 3.6: (a) P-polarized TD-SHG measurement taken with the incident fundamental beam polarization set at 57° , the critical angle for this sample. After about 185 s, the incident fundamental polarization was changed quickly from 57° to 0° (P_{in}). (b) $P_{in} - P_{out}$ measurement from a fresh location on the same sample. The incident plane is parallel to (100) crystal plane. Initially, the laser beam was blocked for the first 10 s.

Therefore a critical angle of a material is the characteristic property of the material which is characterized by $\chi^{(3)}$ in equation (3.1).

P_{out}- and S_{out}-polarized SHG responses were measured as a function of polarization angle after saturation as shown in Fig. 3.7. At each SHG maximum, strong time dependencies were observed. For example, for P-polarized SHG signals strong time-dependencies were shown at $\varphi = 0$, 90, 180 and 270 degrees which are the angles corresponding to the maximum SHG signals. In contrast, at each SHG minimum no time dependencies were observed in each SHG measurement. This confirms that the TD-SHG responses from thin oxide on silicon systems comes almost entirely from the DC electric field induced $\chi^{(2)}$ under broken symmetry through the z-axis.

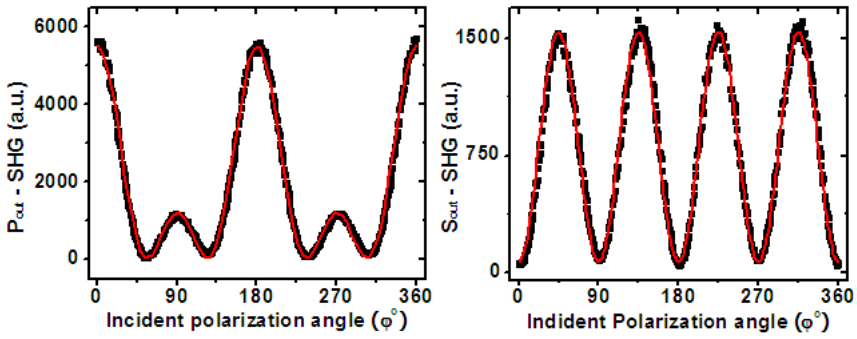

Figure 3.7: P- and S-polarized SHG measurements with respect to incident polarization angle after saturation. The red solid curves are fitting results using Eq. (3.20) and Eq. (3.22). The incident plane is parallel to (100) crystal plane.

3.5 Azimuthal rotational invariance of TD-SHG signals

The experimental results of time-dependent SHG measurements were found to be independent of the sample azimuthal orientation for any given input and output set of polarization angles, i.e., when the samples were rotated about the sample normal, the TD-SHG behaviors were observed to be unchanged as shown in Fig. 3.3. Even the critical angle was not changed as the sample was rotated around the sample normal. This results can be easily accounted for by an analysis of the properties of the $\chi^{(2)}(E_{dc})$ tensor which was derived under the assumption of mirror symmetry through the x or y axes. The $\chi^{(2)}$ of isotropic media is rotationally invariant and has the same tensor form as $\chi^{(2)}(E_{dc})$ expressed in Eq.(3.3) which was derived as a surface tensor for a cubic material. Thus the $\chi^{(2)}(E_{dc})$ is also invariant under sample rotation around the sample normal. However higher order nonlinear optical responses can distinguish the surface symmetry properties between cubic and isotropic media [46]. A mathematical proof of the rotational invariance of the $\chi^{(2)}(E_{dc})$ is given below.

Two rectilinear coordinate systems are defined, a beam coordinate system and a sample coordinate system. The beam coordinate system (x, y, z) is fixed during measurements and completely define the incoming and out-coming beams as shown in

Fig. 3.4. The sample coordinate system (x', y', z) is fixed to the sample. Because the sample is rotated about z axis, the z' axis is the same as z. Before sample rotation, the second order polarization equation is

$$P^{(2)}_{(b)} = \chi^{(2)} : E_{(b)}E_{(b)} \tag{3.24}$$

in the beam coordinate system, where subscript (b) indicates the beam coordinate system. If the sample is rotated by ψ degree around the sample normal, $\chi^{(2)}$ is generally changed and the induced second order polarization is also changed. Therefore we have

$$P^{(2)'}_{(b)} = \chi^{(2)'} : E_{(b)}E_{(b)} \tag{3.25}$$

in the beam coordinate system after rotation. The electric field $E_{(b)}$ is not changed in the beam coordinate system. The second order polarization equation can be written as

$$P^{(2)'}_{(s)} = \chi^{(2)} : E_{(s)}E_{(s)} \tag{3.26}$$

in the sample coordinate system, where the subscript (s) stands for the sample coordinate system and $E_{(s)}$ stands for the fundamental electric field in the sample coordinate system.

$P^{(2)'}_{(s)}$ and $P^{(2)'}_{(b)}$ are the same physical polarizations in the two different coordinate systems after the sample is rotated. We can transform the polarization vectors and the electric field vectors by applying the rotation matrix R(ψ) which is defined by

$$\begin{pmatrix} cos\psi & sin\psi & 0 \\ -sin\psi & cos\psi & 0 \\ 0 & 0 & 0 \end{pmatrix}.$$

After rotating the sample, the electric fields and polarization vectors are transformed as

$$E_{(s)} = R(\psi)E_{(b)} \tag{3.27}$$

and

$$\begin{aligned} P_{(b)}^{(2)'} &= R(-\psi)P_{(s)}^{(2)'} \\ &= R(-\psi)\chi^{(2)} : E_{(s)}E_{(s)} \\ &= R(-\psi)\chi^{(2)}[R(\psi)E_{(b)}][R(\psi)E_{(b)}]. \end{aligned} \tag{3.28}$$

It can be shown that ψ dependent terms in the last part of equation (3.28) cancel out using the $\chi^{(2)}$ expressed in Eq. (3.6), leaving $\chi^{(2)} : E_{(b)}E_{(b)}$. Thus the induced second order polarization is not changed as the sample is rotated around the sample normal. The second order polarization equation

$$P_{(b)}^{(2)'} = \chi^{(2)'} : E_{(b)}E_{(b)} \qquad (after\ sample\ rotation)$$

is the same as

$$P_{(b)}^{(2)} = \chi^{(2)} : E_{(b)}E_{(b)} \qquad (before\ sample\ rotation).$$

Finally it proves $\chi^{(2)} = \chi^{(2)'}$ before and after sample rotation. Any tensor such as

$$\begin{pmatrix} 0 & 0 & 0 & 0 & \chi_1 & 0 \\ 0 & 0 & 0 & \chi_1 & 0 & 0 \\ \chi_2 & \chi_2 & \chi_3 & 0 & 0 & 0 \end{pmatrix}$$

is rotationally invariant for $P^{(2)} = \chi^{(2)}$:EE. Thus the invariance of the critical angle follows from this tensor analysis under the dipole radiation approximation.

3.6 Bulk quadrupole contribution

Though only the dipole radiation approximation is used in the previous analysis, there is clearly a DC electric field enhanced bulk electric quadrupole contribution to the TD-SHG signals. DC field enhanced quadrupole SHG was well characterized by Aktsipetrov et al. [47] in silicon. They used an external bias to create a DC electric field inside silicon samples and observed a four-fold symmetry in SHG under sample rotation. In the thin oxide on silicon system (Wafer 1 in Table 3.1), four-fold

symmetric SHG signals were also observed in $P_{in} - P_{out}$ and $S_{in} - P_{out}$ configurations near SHG saturation. The results are shown in Fig. 3.8.

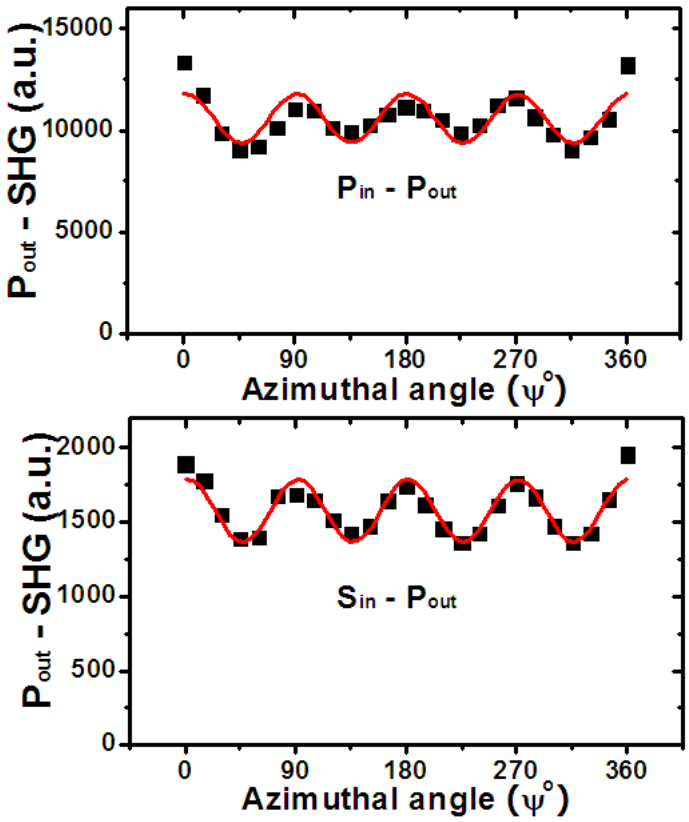

Figure 3.8: RA-SHG measurements in two different beam configurations ($P_{in} - P_{out}$ and $S_{in} - P_{out}$) from wafer 1 in Table 3.1. $\psi = 0°$ corresponds to that the incident plane is parallel to (100) silicon crystal plane. The oscillations arise from an electric quadrapole contribution. Squares are measured data and red curves are fits by Eq. (3.29). Each data point was taken on a new spot after 1 minute at each azimuthal angle measured.

The rotational anisotropic SHG (RA-SHG) results can be fit by the following equation [47]

$$I(2\omega) = c_0 + c_4 cos[4(\psi - \psi_0)]. \tag{3.29}$$

The relative ratios of c_0/c_4 are obtained by the fitting which are found to be 0.11 and

0.13 for $P_{in} - P_{out}$ and $S_{in} - P_{out}$ respectively. For $P_{in} - P_{out}$, this result is consistent with a previous result in thin oxide Si(100)/SiO2 [10]. The fitting results show that the isotropic component c_0 is dominant in the RA-SHG signals. It was observed that the critical angle is also independent of silicon crystalline plane direction. It means that the DC field enhanced quadrupole contribution is negligible at the critical angle. Thus the dipole radiation approximation is a good approach to analyze TD-SHG signals in thin oxide on Si(100) systems. To make the approximation more complete, equation (3.1) may include the bulk electric quadrupole contribution. Therefore it can be expressed as

$$I(2\omega) = \left|\chi^{(2)} + \chi^{(3)} E_{dc} + \chi_{eff}^{(2),BQ}\right|^2 I(\omega)^2, \tag{3.30}$$

where $\chi_{eff}^{(2),BQ}$ is the effective bulk electric quadrupole susceptibility which results in the four-fold anisotropic contribution to the RA-SHG signals.

CHAPTER IV

CHARGE TRAPS IN OXIDE ON SILICON SYSTEMS PROBED BY SECOND HARMONIC GENERATION

This chapter deals with the characterization of boron-induced interface charge traps in Si/SiO2 systems. During the growth of the oxide, boron atoms migrate into the oxide creating charge traps near the interface. The charge traps induce a built-in DC electric field across the interface. It was determined that the direction of the boron induced interface DC electric field is from the oxide to the silicon substrate. The properties of the charge traps are studied by time-dependent SHG measurements [9, 11, 39].

4.1 Characterization of interface charge traps by second harmonic generation

Second Harmonic Generation (SHG) has been utilized as a powerful tool to characterize the properties of material surfaces and the charge status of buried interfaces. Under the dipole radiation approximation, SHG vanishes for inversion symmetric materials such as silicon and amorphous SiO2 [16,40,41]. Therefore surface and interface contributions are the major sources of SHG for such materials. However, when a DC electric field is present inside such materials, SHG is enhanced by a fourth rank tensor contribution, $\chi^{(3)}E_{dc}$ [3, 27, 28, 42, 43]. Electric-field-induced SHG (EFISH) has been used to characterized the interface charge properties of oxide on semiconductor systems. Previously electron and hole dynamics were studied in Si/SiO2 systems using the EFISH method [6, 29]. EFISH was also used to study the interface properties in Si/Al2O3 [30, 31], Si/HfO2 [30, 32], Si/MgO [33], Si/ZrO2 [30, 34], and SOI [35]

systems. In these systems a quasi-static electric field is created arising from the separation of charge carriers.

If the oxide thickness is less than 10 nm in Si/SiO2, the time-dependent SHG (TD-SHG) signal shows a monotonic increase [4, 5]. To characterize the TD-SHG signals in the system, the following equation has been used [5, 6].

$$I(2\omega) = \left|\chi^{(2)} + \chi^{(3)} E_{dc}(t)\right|^2 I(\omega)^2, \tag{4.1}$$

where $\chi^{(2)}$ and $\chi^{(3)}$ are the effective non-linear second- and third-order electric susceptibilities near the Si/SiO2 interface respectively. $E_{dc}(t)$ is a time-dependent quasi-static DC electric field across the Si/SiO2 interface. For accurate description, the " = " sign should be replaced by the proportional symbol " $\propto$ ". However (4.1) is commonly used in experimental analysis. If relatively thin oxides are irradiated with 800 nm wavelength ($h\nu = 1.55$ eV) light, electrons can be exited by a three-photon absorption process above the conduction band of the oxide [6, 44]. These electrons can travel across the oxide to reach the surface of the oxide, leaving the remaining holes near the interface. Finally the electrons may be captured by the ambient oxygen molecules on the surface of the oxide, resulting in the creation of a DC electric field across the Si/SiO2 interface due to the electron-hole pair separation. The increase of the DC electric field can be detected by a EFISH measurement.

4.2 Band offset measurement using two color pump-probe second harmonic generation measurement

Band offset is defined as the energy difference between the conduction/valence band of two different materials. Measuring the band offset of the silicon valence band and the oxide conduction band in Si/SiO2 is very important in silicon based semiconductor applications. The band offset determines the threshold electron energy to inject an electron from the silicon valence band to the oxide conduction band. Internal photoemission (IPE) measurements are commonly used to determine the band offset [48].

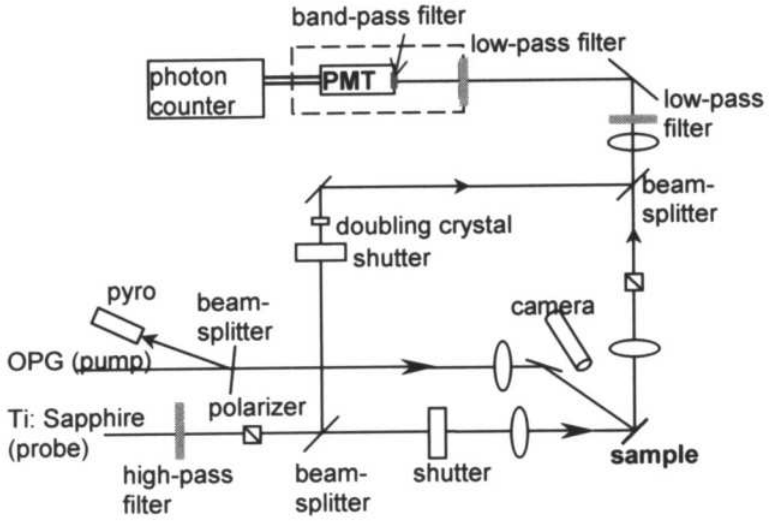

Figure 4.1: Two color pump-probe SHG experimental setup [7].

The measurement predicts the band offset in the range from 4.05 to 4.6 eV.

Marka et at. invented an optical method to measure the band offset using a two-color pump-probe SHG technique [7, 8]. The pump beam had a tunable wavelength output which can excite electrons from the silicon valence band to the oxide conduction band. The probe beam of 800 nm wavelength ($h\nu$ = 1.55 eV) light generated SHG signals from the Si/SiO2 interface which is sensitive to the interface DC electric field. Because the 800 nm wavelength photons also can inject the electrons from the silicon valence band to the oxide conduction band by a three-photon absorption process, the probe beam intensity was significantly reduced to prevent the multi-photon excitation. The experimental setup of the two-color SHG is shown in Fig.4.1. The electrons in the silicon valence band can be excited by a single and multi-photon excitations. A schematic band diagram of Si/SiO2 is shown in Fig.4.2 with single photon and two-photon excitation processes to inject an electron from the silicon valence band to the oxide conduction band.

Depending on the oxide thickness, electrons can tunnel back to the silicon from the oxygen charge traps. For example, if the oxide thickness is about 2 nm, the electrons

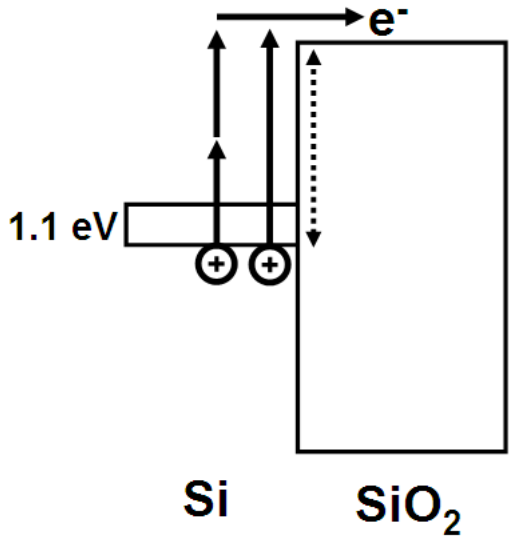

Figure 4.2: A schematic band diagram of Si/SiO2. Dashed arrow: band offset between the silicon valence band and the oxide conduction band. Solid arrows: single photon and two-photon excitations to inject an electron from the silicon valence band to the oxide conduction band.

in the oxygen charge traps tunnel back to the silicon substrate. However, if the oxide thickness is around 4 nm, the excited electrons are trapped in the oxygen charge traps for a while without significant tunneling. This electron trapping and detrapping can be monitored by the EFISH method. An experimental result of the two-color SHG is shown in Fig. 4.3 for a thin oxide (1.7 nm thick) on silicon sample. For the first 200 s, only the 800 nm wavelength probe beam was irradiated onto the sample. Because the probe beam intensity was very weak, electron injection to the surface oxygen traps was negligible. Thus the SHG signal showed almost no time dependency, or a very slow increase. At 200 s, the 800 nm wavelength pump beam was irradiated onto the sample which induced three-photon electron excitations, and then electrons filled the oxygen charge traps resulting in an increasing interface DC electric field. The increasing DC electric field was monitored by the SHG signal of the probe beam. At 730 s, the pump beam was blocked which resulted in the recombination of electron

and hole pairs in the silicon substrate. Therefore slowly decreasing SHG signal was shown after blocking the pump beam.

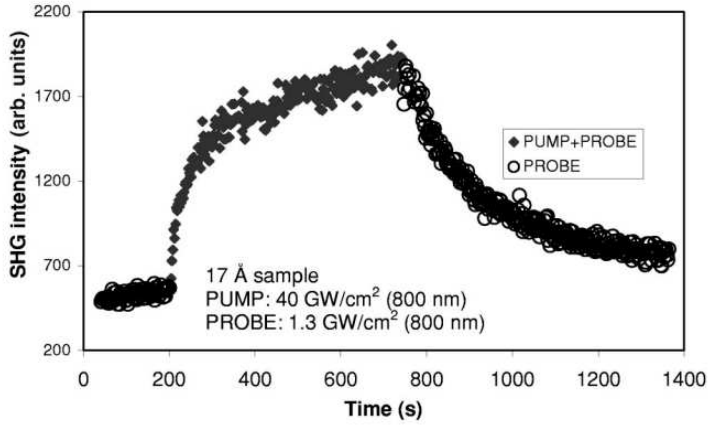

Figure 4.3: Pump-probe time-dependent SHG data for a 1.7 nm oxide [8].

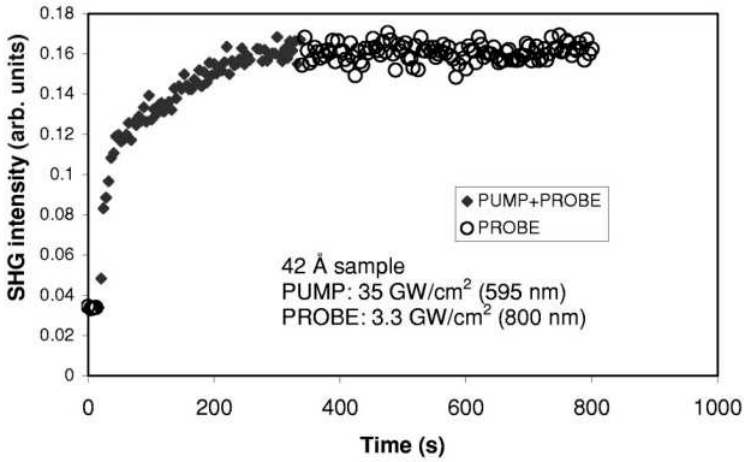

Figure 4.4: Pump-probe time-dependent SHG data for a 4.2 nm oxide [8].

If the oxide is thick enough, the electron-tunneling from the oxygen charge traps can be prevented. In this case, though the pump beam is blocked, the electrons remain in the oxygen charge traps. Therefore no SHG decrease is observed during blocking the pump beam. An experimental result is shown in Fig. 4.4. At 300 s,

the 595 nm wavelength pump beam was blocked and the SHG signal remained at the saturated level which implied that there was no change of the interface DC electric field. This result ensures that the detrapping rate can be ignored from the oxygen charge traps. Thus the rate equation for the electron injection can be approximated only using the electron excitation rate by the pump beam. The rate equation is

$$\frac{dn_e}{dt} = (n_{0e} - n_e)/t^e_{pump}, \tag{4.2}$$

where the n_{0e} is the initial number of the unfilled oxygen charge traps and n_e is the number of the filled oxygen charge traps. The solution of the rate equation is easily obtained as

$$n_e(t) = n_0(1 - e^{-t/t^e_{pump}}), \tag{4.3}$$

and the TD-SHG results can be fit by the following equation

$$I^{(2\omega)}(t) = |a + b(1 - e^{-t/t^e_{pump}})|^2. \tag{4.4}$$

From fitting the experimental results with equation (4.4), the time constant t^e_{pump} can be determined. The multi-photon excitation probability is proportional to the order of the power of the beam intensity which is given by

$$W \propto I^{(n)}, \tag{4.5}$$

where I is the intensity of the incoming beam and n is the order of the number of the photons for the multi-photon excitation [8]. Therefore the number n can be obtained by measuring intensity dependent electron injection rates. One example is given by Fig. 4.5 for a 512 nm wavelength pump beam. It shows a different saturation time depending on the pump beam intensity. The obtained electron injection rate, $1/t^e_{pump}$, is plotted in Fig. 4.6 as a function of the pump beam intensity (pulse energy).

For a 512 nm wavelength pump beam, the number n was shown to be 2.24 which implied that the multi-photon excitation involved two-photon absorption. The order of multi-photon excitation number n was plotted with respect to the wavelength of

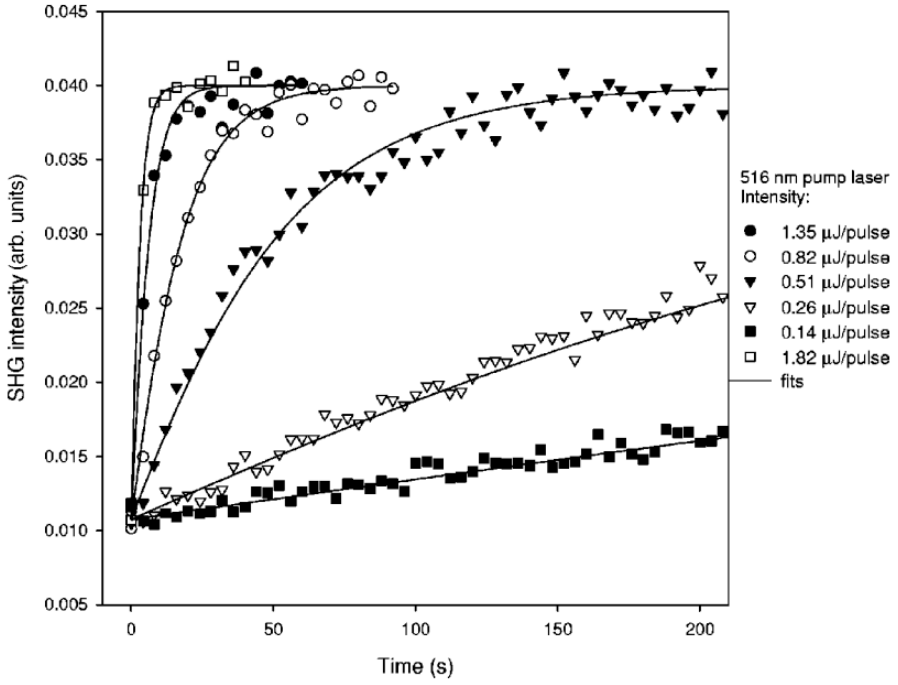

Figure 4.5: TD-SHG measurements in various pump beam intensity for $\lambda_{pump} = 512$ nm [8].

the pump beam in Fig. 4.7. The results showed that there are two thresholds in the photon energy which are for a single photon excitation or multi-photon excitation at the Si/SiO2 interface. The minimum photon energy for the one photon excitation is about 4.5 eV and for a two-photon excitation it is about 2.2 eV. Thus the band offset between the silicon valence band and the oxide conduction band is about 4.5 eV.

4.3 Boron induced interface charge traps in Si/SiO2 probed by second harmonic generation

Recently boron induced interface charge traps were characterized by the TD-SHG approach in highly boron-doped Si/SiO2 systems [9, 10]. A typical TD-SHG signal shows a monotonic increase in thin oxide on silicon systems as shown in Fig 4.8. However the TD-SHG signals in highly boron-doped Si/SiO2 systems showed different

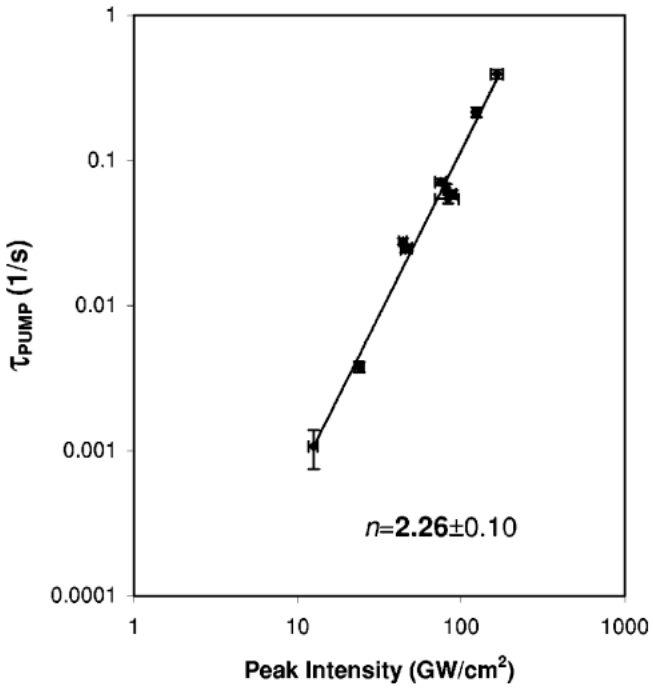

Figure 4.6: Electron injection rate with respect to the pump beam intensity for $\lambda_{pump} = 512$ nm [8].

results from the Sb doped n-type Si/SiO2 systems of Fig. 4.8. They showed an initial sharp decrease in a TD-SHG measurement (Fig. 4.9). Because the temporal variation of the SHG signals in the systems comes from the time-dependent interface DC electric field, the initial sharp decrease in the TD-SHG measurement was attributed to a built-in DC electric field which was induced by boron dopants.

Scheidt, et al., used rotational anisotropic SHG (RA-SHG) measurements to determine the direction of the initial built-in interface electric field [10]. The RA-SHG results showed a phase difference between the initial and saturated SHG signals which is shown in Fig. 4.10. The phase difference confirmed that the boron induced charge traps and the oxygen charge traps create DC electric fields in opposite directions [42]. Therefore the direction of the DC electric filed was determined to be from the oxide towards the silicon substrate.

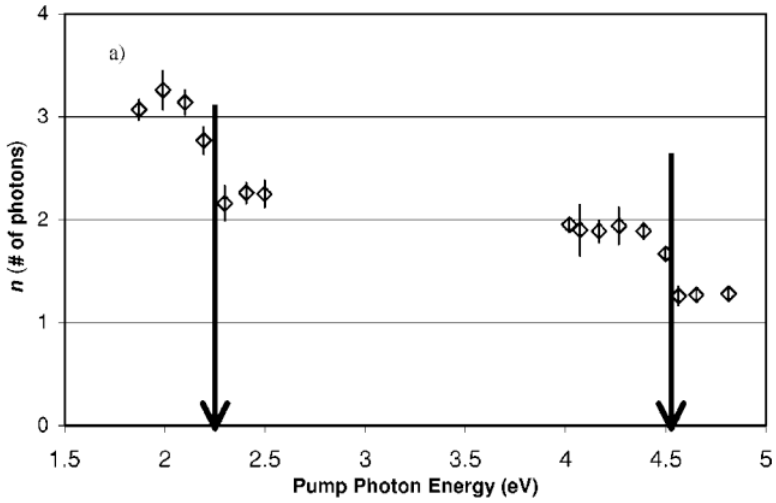

Figure 4.7: The order of multi-photon excitation process to inject electrons from the silicon valence band to the oxide conduction band [8].

We also performed a series of TD-SHG measurements in various silicon wafers and characterized the properties of the boron induced charge traps near the interface of Si/SiO2 [9]. Sample labels, dopant type and resistivity data are specified in Table 4.1.

Table 4.1: Descriptions of silicon wafers.

Wafer label	Dopant	Resistivity Ωcm
Wafer A	Boron	5-15
Wafer B	Boron	0.01-0.02
Wafer C	Boron	0.001-0.009
Wafer D	Antimony	0.005-0.02

All wafers were silicon (100) with native oxide layers. For the TD-SHG measurement, the following experimental conditions were used. A Mira Ti:Sapphire laser was used to generate a P-polarized 800 nm beam. The beam was focused onto the

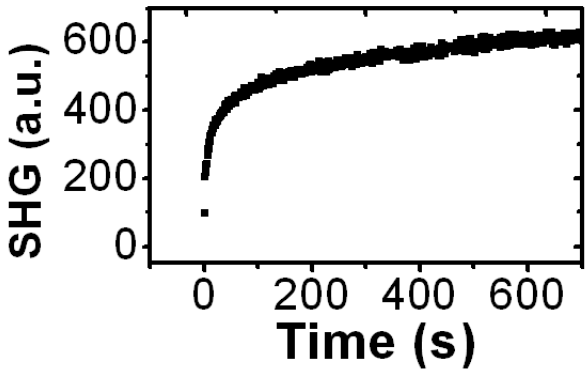

Figure 4.8: TD-SHG measurement in Sb doped Si/SiO2. The oxide thickness is about 2 nm. Resistivity: 0.001-0.02 Ωcm [9].

samples at 45 degrees. The repetition rate of the laser was 75MHz with a pulse width of about 150 fs. Reflected beams were separated by a prism. The frequency-doubled beam (400 nm wavelength) was directed to a photo-multiplier-tube. The intensity of the SHG beam was measured by a photon counter. The samples were aligned so that the plane-of-incidence was always parallel to the (100) silicon crystal plane. When the sample was rotated to the (110) crystal orientation, the same experimental results were observed.

Only the highly boron-doped wafers, B and C, showed an initial marked decrease in TD-SHG measurements. However, wafer A could also show the initial SHG decrease under the right experimental conditions, i.e. during fast data acquisition condition. Because the time-dependency in SHG comes from the DC electric field at the interface of Si/SiO2, the following is suggested. Prior to the laser measurements, a significant electric field is present at the Si/SiO2 interface. This field can be attributed to the presence of B- ions in the silicon substrate and B+ ion in the oxide, which forms a capacitor-like field near the interface. The initial SHG signal at t = 0 comes from the combination of $\chi^{(2)}$ and $\chi^{(3)}E(t=0)$ as shown in equation (4.1), where E(t=0) is the initial DC electric field at the interface. This initial DC electric field arises

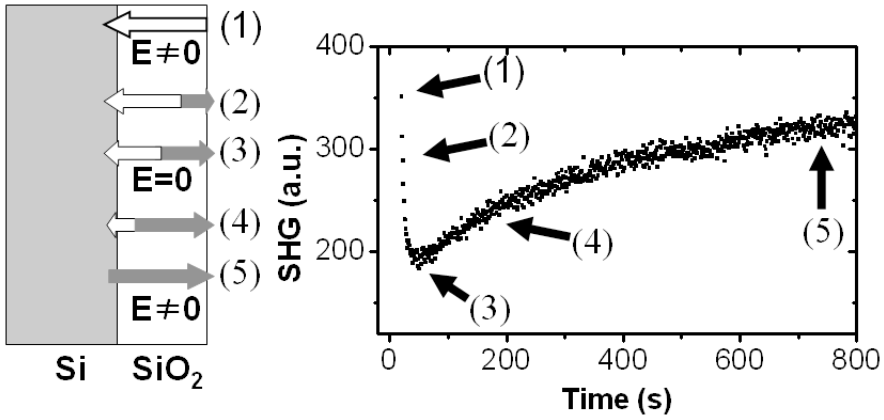

Figure 4.9: TD-SHG measurement in Boron doped Si/SiO2. The oxide thickness is about 2 nm. Resistivity: 0.001-0.009 Ωcm [9].

from boron induced charge traps as indicated by (1) in Fig. 4.9. The direction of the built-in DC electric field is from the SiO2 to the silicon substrate. During the laser irradiation, photo-exited electrons may both fill the boron B+ charge traps and travel through the oxide and be captured by ambient oxygen charge traps on the surface of the oxide. For the first case, the electrons captured by the B+ charge traps decrease the magnitude of the initial DC electric field. For the second case, filling the oxygen charge traps, a time-dependent capacitor like field is created opposite to the direction of the initial boron-induced DC electric field. Thus, the net electric field decreases as indicated by the decreasing SHG signal as shown by (2) in Fig. 4.9. At the minimum of the TD-SHG signal, the net electric field becomes zero though the two separate electric fields may not be zero as indicated by (3) in Fig. 4.9. After reaching a minimum SHG level, the SHG signal increases as more electrons are transferred onto the oxygen molecules on the oxide surface and onto the B+ charge traps until both are saturated, as shown in (4),(5) in Fig. 4.9. Because the oxide layer is relatively thin, oxygen charge traps can release electrons easily. When the laser beam is blocked, the electrons in the oxygen molecules can tunnel back to the empty states in the valence band of the silicon substrate, which results in a decrease of the DC electric field at

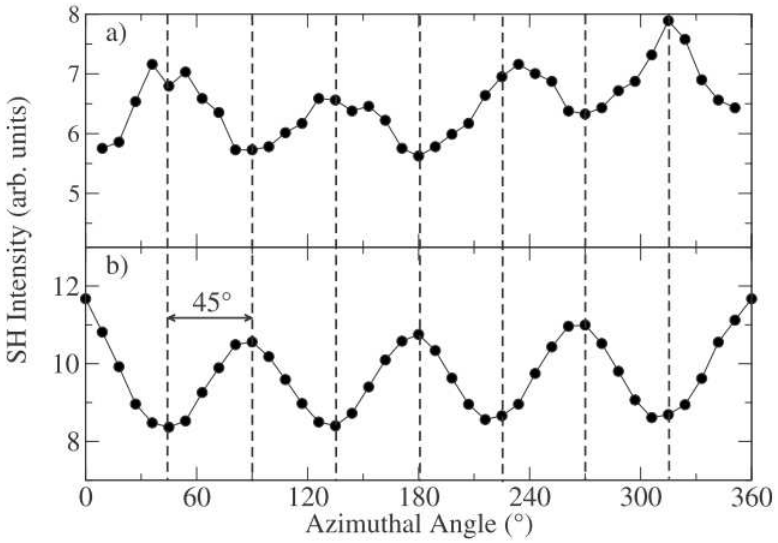

Figure 4.10: RA-SHG measurements for the initial SHG(upper) and saturated SHG (down) signals. 45° phase shift between the two measurement [10].

the interface.

Electrons in the filled boron charge traps may be released and move back to the silicon substrate if the incoming laser beam is blocked. In this case the sharp initial SHG signal should be recovered. However, when the beam was unblocked after blocking the beam for a short period (a few minutes), no initial SHG decrease was observed. Even after a long blocking time (more than one hour), no significant recovery of the originally observed SHG decrease was observed. If the beam was blocked for more than several hours, a discernable recovery was observed. This recovery may come from the released electrons or slight laser beam shift. But in any case no complete SHG recovery was observed. Thus we may infer that the electron detrapping rate for the boron charge traps is much less than the electron detrapping rate for the surface oxygen traps.

The experimental result shown in Fig. 4.11 shows negligible recovery of the initial SHG signal. Initially the laser beam was blocked for 10 s. 10 s later the SHG measurement is begun from a fresh sample location. It showed that a strong sharp

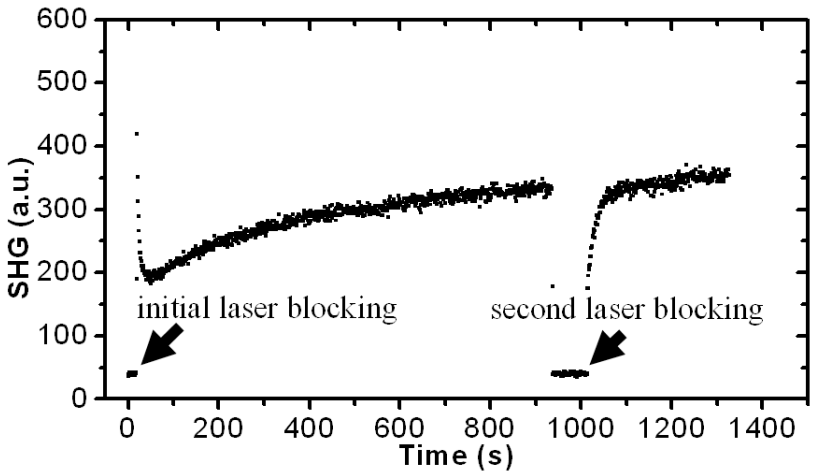

Figure 4.11: TD-SHG measurement from a highly boron doped silicon. During the measurement the laser beam was blocked [9].

decrease resulting from filling the boron induced charge traps and the oxygen traps simultaneously. After saturation, the laser beam was blocked again for about 100 s. When the SHG measurement resumed, the signals did not show any initial decrease which implies that the boron traps did not release the electrons back to the silicon.

4.4 Creation mechanism of boron induced interface charge traps in Si/SiO2

The previous interpretation is supported by a theoretical calculation which showed that neutral boron is more stable in SiO2 than positively ionized boron [49]. Prior to this theoretical work, it was suggested that B atoms diffuse into SiO2 as B+ ions [50]. More recently another group showed that B has various stable and meta-stable forms in Si/SiO2 and they also showed that B+ is one of the stable forms [51, 52]. It is a well-known experimental result that when oxide grows in silicon, most boron atoms migrate into the oxide near the interface. Typically it is described by a segregation coefficient m, which is defined by

$$m = \frac{concentration\ of\ impurities\ in\ silicon}{concentration\ of\ impurities\ in\ oxide}. \tag{4.6}$$

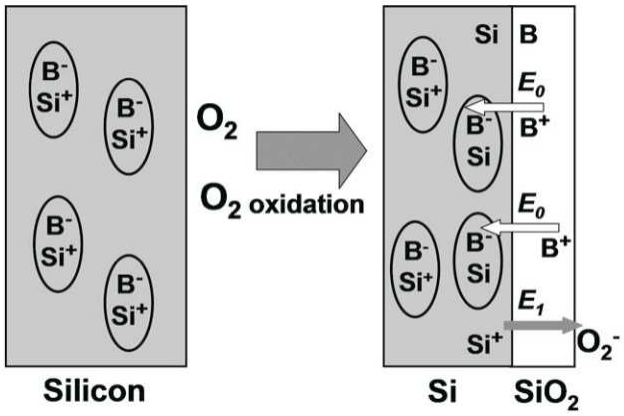

Figure 4.12: Creation of boron induced charge traps in a boron-doped silicon wafer during oxidation (white arrows indicate the electric field by the boron induced charge traps) and photo-injected electron-induced oxygen charge traps (dark arrow indicates the electric field induced by the oxygen charge traps) [9].

For silicon, only boron has a segregation coefficient smaller than one (m $<$ 1) [53]. Based on our measurements and on the theoretical calculations involving the segregation coefficient of boron, we suggested a mechanism for the creation of the boron positive charge traps in the oxide. At room temperature, a boron atom may be easily ionized by acquiring an electron from a silicon atom leaving a hole state in the silicon atom. During the growth of silicon oxide on the silicon substrate, most boron atoms near the interface migrate into the oxide as a neutral state near the interface. But some of the boron atoms in the oxide are ionized as positive ions leaving an electron in the silicon substrate. The electron can occupy the hole state of the silicon or an acceptor state of a neutral boron atom in the silicon substrate. Therefore across the interface negative charges and B+ ions are formed in the silicon and the oxide respectively. This charge formation mechanism is illustrated in Fig. 4.12. These charge traps are responsible for the initial built-in DC electric field which can be detected by TD-SHG measurement.

4.5 Filling the two charge traps simultaneously and independently by changing beam intensity

Because the electron injection to the oxygen charge traps on the oxide surface requires three-photon excitation process, a highly intense beam should be used to create the multi-photon process [5]. When the three-photon excitation occurs, both charge traps are filled simultaneously as shown in Fig. 4.12 and 4.13-uppper blue data. However, when the incoming laser beam power is below 200 mW, no time-dependency in the SHG signals was observed in the N-type (Sn doped) silicon sample. In this manner, we can fill the boron induced traps first, and then fill the oxygen charge traps. As shown in Fig. 4.13 (red data). At the beginning of the measurement, the laser power was 174 mW and the photo-injected electrons filled only the boron induced charge traps which was indicated by the monotonic decrease. While blocking the laser beam the laser power was increased to 345 mW. When the laser beam was unblocked again, the photo-injected electrons filled the oxygen charge traps inducing the E_1 electric field in Fig. 4.12 (dark arrow). Because the boron induced charge traps were filled previously by the low power laser beam, the initial decrease was not observed.

4.6 Boron concentration dependent charge traps and interface effective $\chi^{(2)}$

Our measurement showed that there was a clear difference in the magnitude of the initial decrease in the SHG measurement depending on boron doping concentration as shown in Fig.4.14 - a,b. When the laser power is high enough, the initial SHG decrease cannot be observed for the wafer B since the oxygen traps are occupied very quickly as shown in Fig.4.14-(a):396 mW. However at low laser power, the oxygen charge traps have a very low probability of occupation to be filled by the electrons. Thus only the decrease of the boron-induced electric field is observed shown in Fig.4.14-(a): 154 mW, and (b): 155 mW.

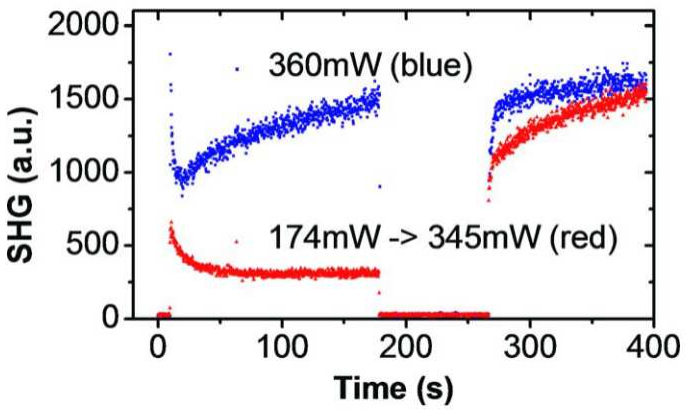

Figure 4.13: Filling the both traps simultaneously (blue, upper graph) and filling the boron induced charge traps first then filling the oxygen charge traps (red, lower graph) from wafer C. The oxide thickness is about 2 nm. Resistivity: 0.001-0.009 Ωcm. Initially the laer beam was blocked for 10 s [9].

Numerical fitting was performed based on equation (4.1) to obtain the relative information of the susceptibilities of wafer B and wafer C, and also the time constants of the charge traps. For intrinsic silicon wafer, $\chi^{(2)}$ and $\chi^{(3)}$ can be considered as real numbers because both $\chi^{(2)}$ and $\chi^{(3)}$ come effectively from a few atomic layers at the interface and absorption is very low at 800 nm wavelength light. However, when the wafer is highly doped, they cannot be considered as real numbers. If the susceptibilities are real numbers, equation (4.1) cannot fit the results and the SHG minimum should be zero. In general, the $\chi^{(2)}$ and $\chi^{(3)}$ can be considered as complex numbers and equation (4.1) can be modified as

$$I(2\omega) = \left||\chi^{(2)}| + |\chi^{(3)}|e^{i\theta}E_{dc}(t)\right|^2 I(\omega)^2, \tag{4.7}$$

where θ is a relative phase between $\chi^{(2)}$ and $\chi^{(3)}$. The time-dependent electric field $E_{dc}(t)$ can be expressed by

$$E_{dc}(t) = E_0 e^{-t/t_1} - E_1(1 - e^{-t/t_2}), \tag{4.8}$$

where E_0 is the magnitude of the initial DC electric field from the boron induced charge traps, E_1 is the magnitude of the DC electric field from oxygen charge traps,

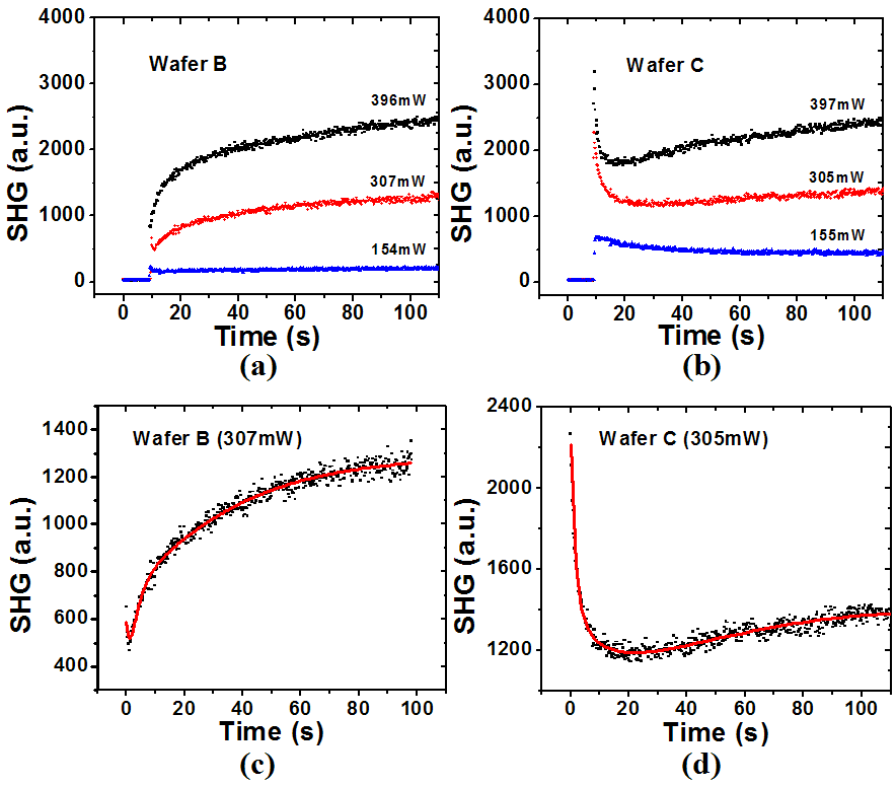

Figure 4.14: (a) TD-SHG results of the wafer B in three different laser powers. (b) TD-SHG results of the wafer C in three different laser powers. (c) Fitting result of 307 mW data of (a). (d) Fitting result of 305 mW data of (b). [9]

t_1 is the detrapping time constant of the boron induced charge trap and t_2 is the trapping time constant of the oxygen charge traps. For accurate fitting, electron detrapping from the oxygen traps should also be considered. However, if only the effective magnitude of $|\chi^{(2)}|$ is considered, introducing a detrapping constant, t_3, does not change the value of $|\chi^{(2)}|$. Separate values of $|\chi^{(3)}|$ cannot be obtained from the fitting because $|\chi^{(3)}|$, θ and $E_{dc}(t)$ are always coupled. In Fig.4.14-(a,b), the two data sets (307 mW and 305 mW) are fitted by the equations, (4.7) and (4.8).

The fitting result indicates that the effective magnitude of $\chi^{(2)}$ depends on the boron doping concentration. As the doping concentration increases, $|\chi^{(2)}|$ also increases. A Van der Pauw four-point-probe experiment was used to measure more

accurate resistivity values of wafers B and C. The resistivity values are 0.0165 Ωcm and 0.00519 Ωcm, respectively. We observed that the effective $|\chi^{(2)}|$ increased in non-linear manner with respect to the boron concentration by comparing relative ratios,

$$\frac{|\chi^{(2)}|_{waferC}}{|\chi^{(2)}|_{waferB}} = 1.55, \tag{4.9}$$

$$\frac{n_{waferC}}{n_{waferB}} = 4.72. \tag{4.10}$$

4.7 TD-SHG in highly boron doped Si/SiO2 with a thermally grown thick oxide layer

If the oxide thickness is greater than 10 nm, excited electrons from the silicon valence band cannot reach the surface of the oxide. In this case, the oxygen charge traps do not play a role in TD-SHG signals. The excited electrons will fill only boron charge traps resulting in a decrease of the built-in DC electric field due to the filling. Therefore for highly boron-doped Si/SiO2 with a thick oxide layer, it is expected that only the boron charge traps are involved in a TD-SHG measurement and a monotonic decrease should be shown in the measurement. An experimental result is shown in Fig. 4.15 using a wafer C with a thermally grown oxide layer (oxide thickness: 12 nm). It showed a monotonic decrease even with a high laser beam intensity (526 mW) resulting from only filing the empty boron induced charge traps in the oxide with the excited electrons in the silicon.

4.8 Determination of a threshold photon energy to fill the boron induced charge traps near the Si/SiO2 interface

Previously, experimental evidences were shown for the presence of boron induced charge traps in Si/SiO2 systems. The charge traps were attributed to the boron ions, B- in the silicon substrate and B+ in the oxide. This suggests that there might be a single energy level for the B+ trap in the oxide which can be filled by a photo-excited

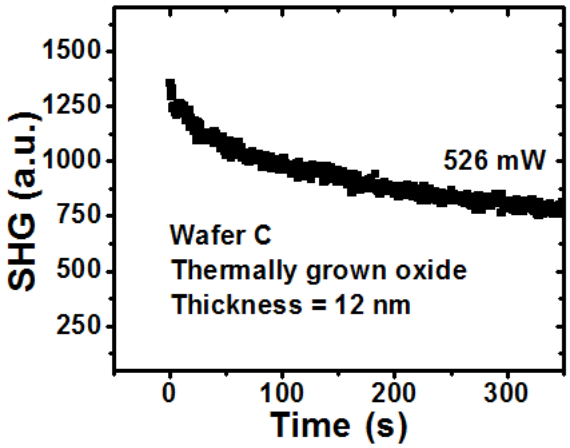

Figure 4.15: A TD-SHG result in highly boron-doped Si/SiO2 with a thermally grown oxide layer (oxide thickness: 12nm, resistivity: 0.001-0.009 Ωcm) [11].

electron. Experimental evidence is shown in this section for the single energy level of the B+ charge traps by determining a threshold photon energy level to fill the traps.

To determine the threshold photon energy, two color pump-probe SHG technique was employed. The experimental configuration is shown in Fig. 4.16. This experimental method was developed previously by our group to characterize X-ray radiation enhanced electron transport in SiO2 [7] and to measure band-offset of Si/SiO2 [8]. In this method, a Ti:Sapphire laser was used as a probe beam (λ = 800 nm) to measure SHG signals from boron-doped Si/SiO2 samples. The peak power of the laser was about 4.6 GW/cm^2 on sample surfaces with a 75 MHz repetition rate and a pulse width of about 150 fs. The 800 nm fundamental beam was P-polarized and P-polarized SHG signals were measured by a photo-multiplier tube (PMT) with a photon counter. The incident angle of the fundamental beam was 45°. An optical parametric amplifier (OPA) was used as the pump beam which has a tunable wavelength beam (λ = 350 - 1400 nm) with a 1 KHz repetition rate. The pump beam was linearly polarized and directed onto the samples very near the normal direction (less than 0.55° incident angle) with respect to the sample surface. The pump beam

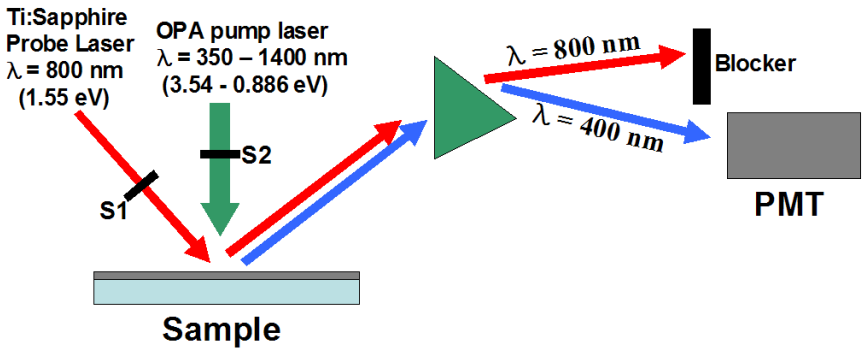

Figure 4.16: Schematic diagram of the two-color pump-probe SHG experiment configuration. S1 and S2 indicate the shutters of the beams.

polarization direction was parallel to (100) silicon crystal plane. Pump beam power was between 7.1 and 9.1 mW during the irradiation. The corresponding peak intensity of the OPA pump beam was approximately 0.18 - 0.14 GW/cm^2 on the sample surfaces. A highly boron-doped silicon (100) wafer was used with resistivity in the range of 0.001-0.009 Ωcm. The thickness of the oxide layer was about 2 nm measured by ellipsometry. All measurements were performed at room temperature.

With sufficient photon energy, the OPA pump beam excites electrons from the silicon valence band to fill the boron charge traps in the oxide. It modifies the interface charge state resulting in the change of the interface DC electric field. The change of the DC electric field can be probed by TD-SHG measurements. The time dependency arises from a quasi-static interface DC electric field arising from a time dependent charge separation across the interface. The TD-SHG intensity is given by equation (4.1). When the probe beam is incident on the surface, the probe beam monitors the interface DC electric field by a SHG signal and simultaneously also fills the charge traps (boron induced charge traps and oxygen charge traps) by exciting the electrons.

There are three possible mechanisms that might account for the filling of boron

charge traps as shown in Fig. 4.17. First, the electrons can be excited below the conduction band of the oxide and at or above the energy level of the B+ traps. In this case, the excited electrons can fill the boron charge traps directly (mechanism I). Second, electrons are excited above the conduction band of the oxide. In that case the electrons can fill the B+ traps during traveling through the oxide (mechanism II). Third, excited electrons may be captured by the oxygen charge traps on the surface of the oxide. If the oxide is thin enough, the captured electrons can tunnel back to the silicon substrate. During the tunneling, the electrons can fill the B+ traps (mechanism III).

Because the probe beam photon energy is 1.55 eV (λ = 800 nm), three-photon absorption is required to fill the oxygen traps. The electron injection by the three photon absorption can be significant only if the incoming fundamental beam is intense enough. In case of low intensity of laser beam, a TD-SHG signal from the highly boron-doped Si/SiO2 shows a monotonic decrease as shown previously, in which only the boron induced charge traps are filled. On the other hand, the TD-SHG result shown in Fig.4.9 may involve all of the three mechanisms resulting in the filling of the boron charge traps.

If two-photon absorption is involved in the photon energy range from 2.25 to 4.5 eV (λ = 550 - 276 nm), the silicon valence band electrons can be excited to reach the conduction band of the oxide and the oxygen charge traps can be filled with the electrons [8]. Thus the boron charge traps may be filled by all of the mechanisms if the beam intensity is sufficient. In our experiment we intended for the OPA pump beam to excite the silicon valence band electrons to fill the B+ traps primarily by single photon absorption. Thus the B+ traps are filled only by the mechanism I. To prevent the multi-photon excitation, the OPA pump beam was unfocused and intensity was significantly reduced using a neutral density filter. The following is a simple experimental procedure.

1: Initially, shutter S1 remains closed thus removing the probe beam.

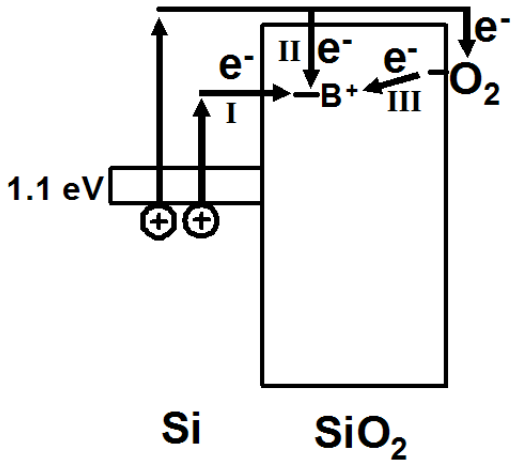

Figure 4.17: Schematic band diagram of three possible mechanisms (I,II,III) for filling boron charge traps.

2: Shutter S2 remains open for 15 minutes to irradiate the sample by the pump beam.

3: Shutter S2 is closed.

4: Shutter S1 is then opened for a TD-SHG measurement.

The step 4 procedure was performed within 1 minute after the step 3 procedure. The filled boron charge traps were observed to be quite stable or at least have a very long recovery time, we used fresh sample locations for each measurement.

A strong pump wavelength dependence was observed in the TD-SHG measurements as shown in Fig. 4.18. When a 350 nm ($h\nu = 3.54$ eV) pump beam was directed onto a sample, the initial SHG signal was significantly decreased. However, when a 700 nm ($h\nu = 1.77$ eV) pump beam was used, there was no significant decrease in the initial SHG signal, which was essentially an identical to an TD-SHG data of a fresh sample location where no pump beams was applied. This result indicates that there exists a threshold photon energy to fill the B+ traps. To analyze this wavelength dependent electron filling effect quantitatively, the minimum SHG intensity was defined

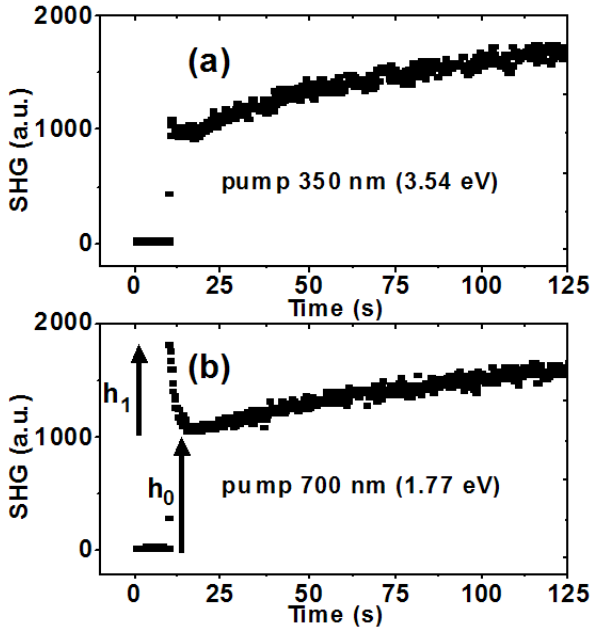

Figure 4.18: TD-SHG measurements after irradiating OPA pump beams with (a) 350 nm and (b) 700 nm light. Initially, the probe beams were blocked for the first 10 s.

to be h0 and the initial decrease in SHG intensity to be h1. The relative ratios of h1/h0 are plotted as a function of the OPA pump beam photon energy in Fig. 4.19.

Our data show a striking threshold photon energy at 2.61 eV ($\lambda = 475$ nm). If the pump beam photon energy is less than 2.61 eV, the pump beam does not change the interface charge state by single photon absorption. Our experimental results strongly suggest that electron trapping energy level is formed in the oxide near the interface at 2.61 eV above the silicon valence band. This trap energy level can be filled directly with an excited electron by single photon absorption process if the photon energy is greater than 2.61 eV. Because silicon has an indirect band-gap, if an electron is excited by a photon which has higher energy than 2.61 eV but smaller energy than 3.4 eV, phonon assistance may be involved to fill the boron charge traps which is shown by the dashed arrows in Fig. 4.20.

Though we identified the boron induced charge traps in SiO2 as B+ ions, it

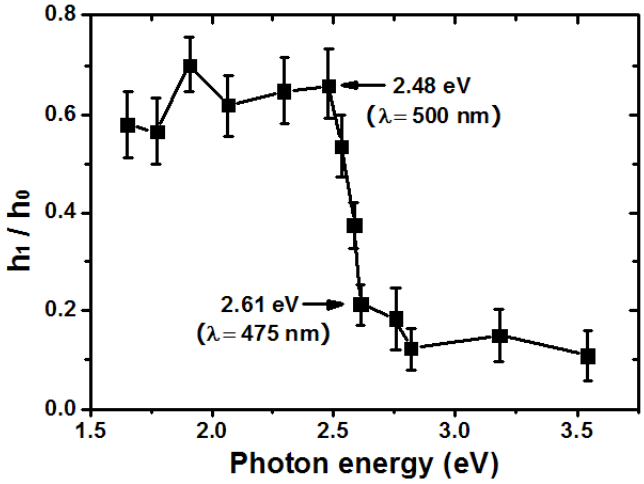

Figure 4.19: Relative comparison of h1/h0 with respect to the photon energy of OPA pump beam.

should be pointed out that there can be other types of charge traps in the oxide induced by the boron migration. When a B+ ion or B atom migrates into the oxide layer, they may capture one or two electrons from Si or O atoms making positively charged Si or O which creates different types of charge traps in the oxide. They may have different energy levels. This possibility can be deduced from the theoretical calculations which found various stable forms of boron atoms in SiO2 [51, 52]. In addition, our measurements show that the B+ charge trap has a very deep energy level in the oxide. This is in contrast to the electrical measurement of a trap energy level of boron, we assume a B+ structure, in SiO2 in a MOS structure [54], which predicted a very shallow boron induced trap energy level, approximately 0.56 eV below the oxide conduction band. This difference may come from an interface effect. Our optical method reveals the trap energy level very near the interface, while the electrical method measured an average trap energy level through the whole oxide layer. The discrepancy may also come from a non-abrupt energy level change in the oxide within 0.5 nm range from the interface which was suggested by a theoretical calculation [55].

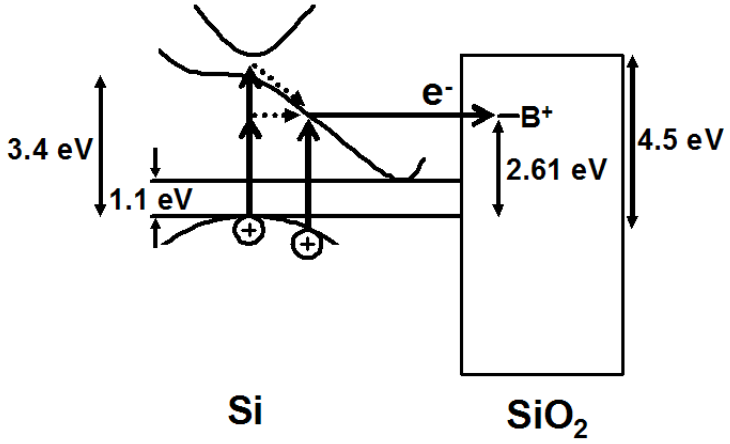

Figure 4.20: Schematic diagram of possible single photon excitation processes resulting in the filling of boron charge traps. Dashed arrows correspond to phonon assisted processes.

CHAPTER V

SUMMARY

Chapter one includes a brief history of the development of the basic principles of nonlinear optics, and second harmonic generation (SHG). Electric field induced second harmonic generation (EFISH) is explained in chapter two as an application of nonlinear optics. EFISH is a very sensitive tool to characterize the charge state of the surface and interfaces in centro-symmetric materials such as silicon and amorphous materials. This is possible because the bulk second order nonlinear response vanishes in the dipole radiation approximation.

In chapter three, polarization-dependent temporal behaviors of SHG in Si/SiO2 systems are characterized theoretically and experimentally. A tensor formulism is developed to explain the experimental results. Within the dipole radiation approximation, all of the time-dependent SHG (TD-SHG) results can be explained by this newly formulated tensor formulism. However, rotational anisotropic SHG (RA-SHG) measurements suggested that there are higher order nonlinear contributions to the TD-SHG signals, which mainly arise from bulk electric quadrupole radiation originating in the silicon substrate. The validity of the dipole radiation approximation is discussed at the end of the chapter and the RA-SHG results showed that the approximation is a good approach within about 10 % error for the systems. A critical polarization angle was determined for these systems for which no time variation was observed in the P-polarized SHG signals. The critical angle is found to be independent of oxide type, dopants, doping concentration and also oxide thickness. These results suggest that the critical angle may be a characteristic parameter of particular materials which can be a useful tool to characterize material properties.

The TD-SHG optical technique has been utilized to characterize the interface properties of Si/SiO2 systems. In particular, boron induced charge traps are characterized by using this method as discussed in chapter four. Experimental results show that boron impurities create a significant built-in DC electric field at the interface of Si/SiO2 systems during the growth of the oxide. The direction of the DC electric field was found to be from the oxide to the silicon. A charge formation mechanism was proposed based on the migration properties of the boron atom near the interface. From the TD-SHG measurements it is shown that the boron charge traps are very stable after being filled by excited electrons. Utilizing a two-color pump-probe SHG experiment, a threshold photon energy was found to fill the boron induced charge traps near the interface by single photon excitation. The threshold single photon energy was found to be 2.61 eV. Efforts to explain this phenomena are in progress.

APPENDIX A

Material properties of silicon

* All data for silicon are from "http://www.ioffe.rssi.ru/SVA/NSM/Semicond/"

1.1 Basic material parameters of Si at 300 K

Crystal structure: Cubic diamond

Number of atoms per 1 cm^3: 5×10^{22}

Density: 2.329 g/cm^3

Dielectric constant: 11.7

Electron affinity: 4.05 eV

Lattice constant: 0.5431 nm

Optical phonon energy: 0.063 eV

1.2 Band structure of Si

Energy gap: 1.12 eV (indirect)

Intrinsic carrier concentration: $1 \times 10^{10} cm^3$

Intrinsic resistivity: $3.2 \times 10^5 \Omega cm$

Effective conduction band density of states: $3.2 \times 10^{19} cm^{-3}$

Effective valence band density of states: $1.8 \times 10^{19} cm^{-3}$

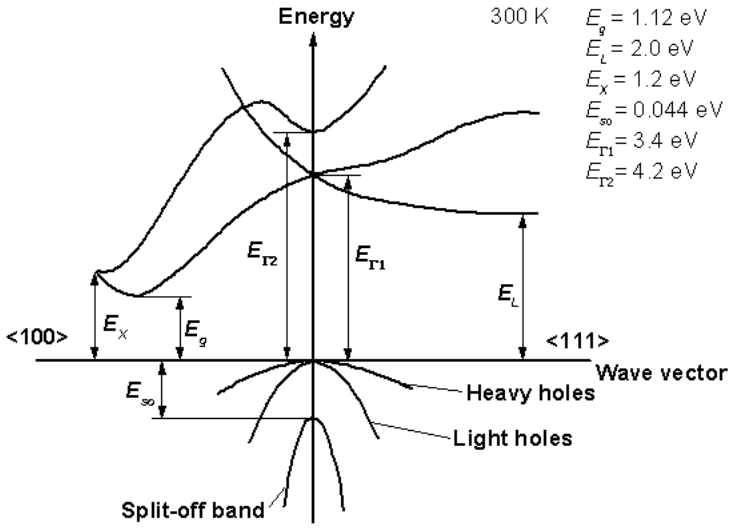

Figure 1.1: Band structure of silicon.

1.3 Electrical properties of Si

Breakdown field: $\approx 3 \times 10^5 V/cm$

Electron mobility: $\leq 1400 cm^2 V^{-1} s^{-1}$

Hole mobility: $450 cm^2 V^{-1} s^{-1}$

1.4 Optical properties of Si

Static dielectric constant: 11.7 at 300 K

Infrared refractive index: n = 3.42 at 300K

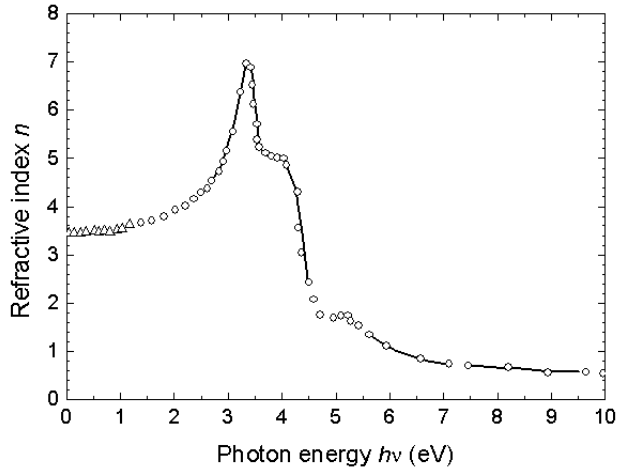

Figure 1.2: Refractive index of silicon at 300 K.

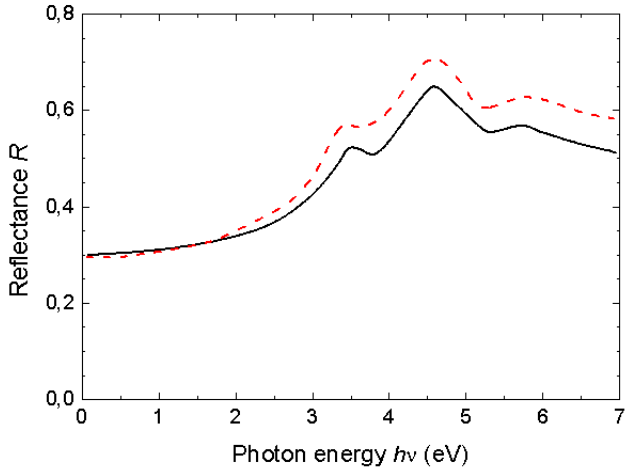

Figure 1.3: Reflectance of silicon. (dashed line: experimental, solid line: theory)

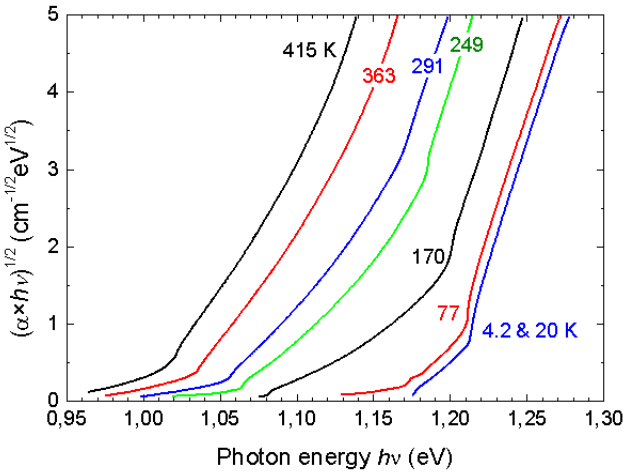

Figure 1.4: Absorption coefficient of silicon at various temperatures.

APPENDIX B

Material properties of amorphous SiO2

Structure: amorphous

Density: 2.2 g/cm^3

Dielectric constant: 3.9

Refractive index: 1.46 at 800 nm

Energy band gap: 9 eV at 300 K

* From http://www.siliconfareast.com/sio2si3n4.htm

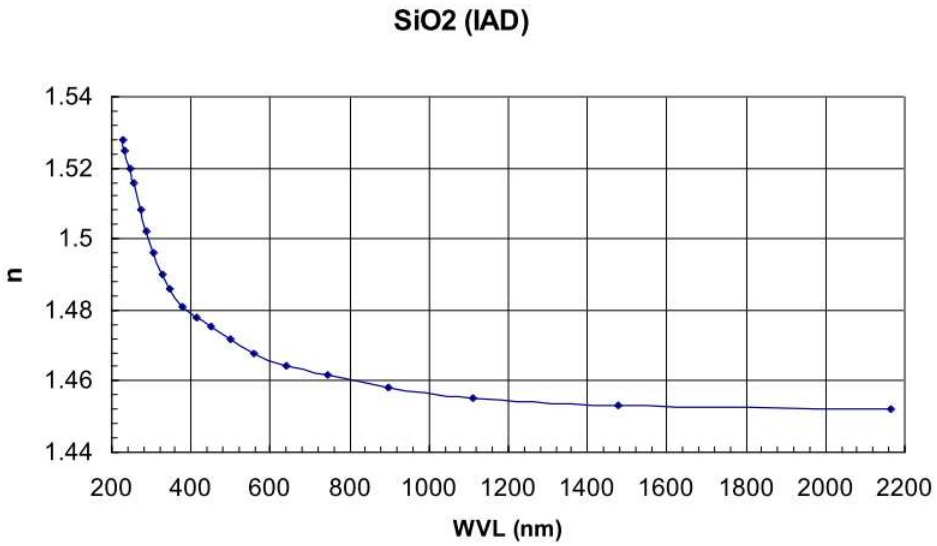

Figure 2.1: Refractive index of SiO2 at 300 K. From 'www.cerac.com'

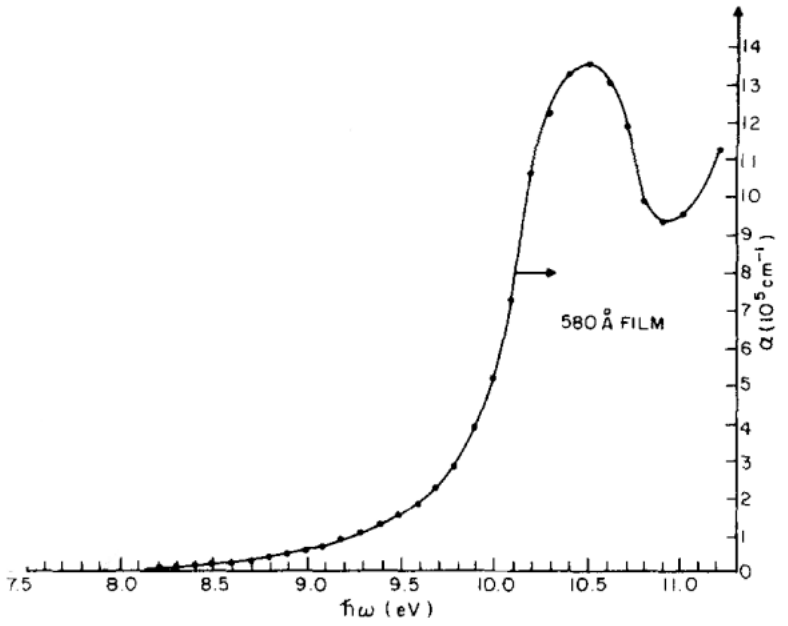

Figure 2.2: Absorption coefficient of thermally grown SiO2 with respect to photon energy. From J. Appl. Phys. 49, 2499 (1978)

APPENDIX C

Photo-Multiplier Tube (PMT) description

Because the light intensity of second harmonic generation (SHG) in Si/SiO2 is very low, a highly sensitive photo detector is required to measure the intensity. For my SHG experiment, a PMT (R4632 model) from Hamamatsu Photonics was used.

PMT is the most sensitive light detector. It can detect even a single photon. A PMT consists of mainly three parts: photocathode, dynodes and anode. The basic working principle of a PMT is shown in Fig. 3.1. When light enters the photocathode, photoelectrons are emitted. The emitted electrons are collimated by a focusing electrode directing into the dynodes. The number of electrons are multiplied in each dynode. Finally, the multiplied electrons are collected by the anode which can be measured as an electric signal. The quantum efficiency of the photocathode is strongly dependent on the wavelength of light. An actual picture of the R4632 model PMT is shown in Fig. 3.2 and the quantum efficiency of the photocathode is shown in Fig. 3.3.

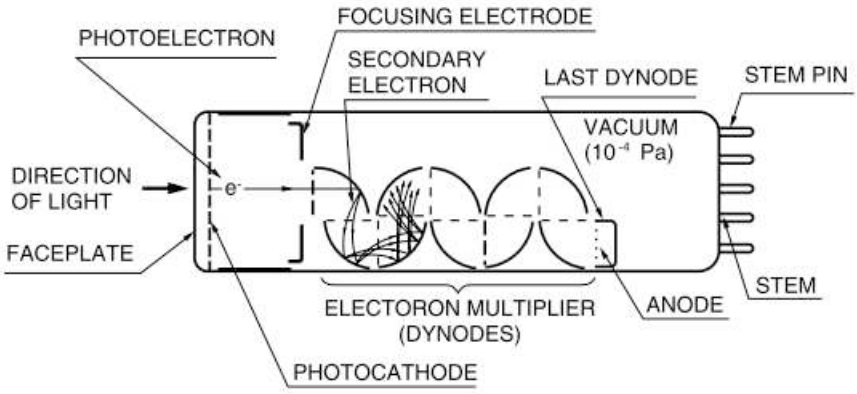

Figure 3.1: Schematic diagram of head-on type photo-multiplier tube (PMT). From 'hamamatsu.com'

Figure 3.2: A picture of R4632 side-on PMT. From 'hamamatsu.com'

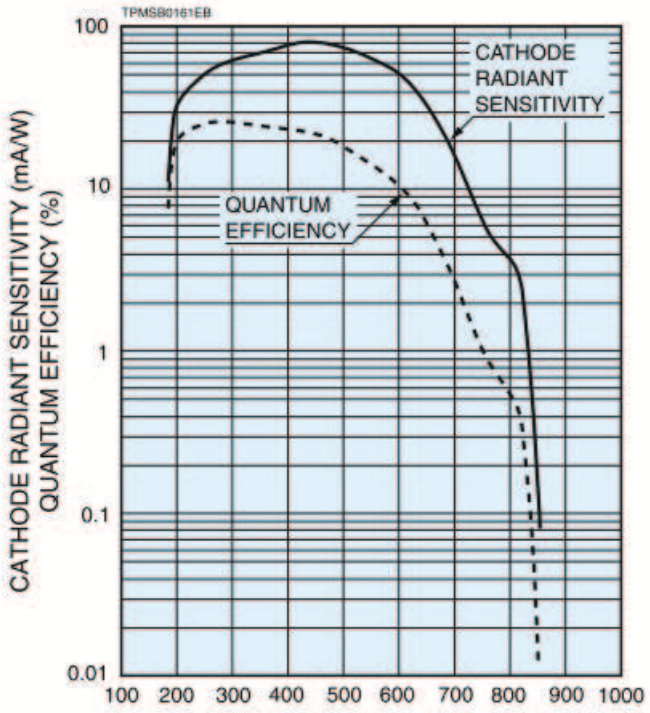

Figure 3.3: Spectra response of R4632 PMT. From 'hamamatsu.com'

BIBLIOGRAPHY

[1] P. Franken, A. Hill, C. Peters, and G. Weinreich, Physical Review Letters **7**, 118 (1961).

[2] C. Lee, R. Chang, and N. Bloembergen, Physical Review Letters **18**, 167 (1967).

[3] O. Aktsipetrov et al., Physical Review B **54**, 1825 (1996).

[4] J. G. Mihaychuk, J. Bloch, Y. Liu, and H. M. van Driel, Optics Letters **20**, 2063 (1995).

[5] J. Bloch, J. Mihaychuk, and H. van Driel, Physical Review Letters **77**, 920 (1996).

[6] W. Wang et al., Physical Review Letters **81**, 4224 (1998).

[7] Z. Marka et al., Journal of Applied Physics **93**, 1865 (2003).

[8] Z. Marka et al., Physical Review B **67** (2003).

[9] H. Park et al., Applied Physics Letters **95**, 062102 (2009).

[10] T. Scheidt, E. G. Rohwer, P. Neethling, H. M. von Bergmann, and H. Stafast, Journal of Applied Physics **104**, 083712 (2008).

[11] H. Park et al., Physica Status Solidi (b) **To be published** (2010).

[12] H. Tom, T. Heinz, and Y. Shen, Physical Review Letters **51**, 1983 (1983).

[13] C. Teplin and C. Rogers, Physical Review B **65** (2002).

[14] R. Boyd, *Nonlinear optics*, Academic Press, San Diego CA, 2nd ed. edition, 2003.

[15] M. Fox, *Optical properties of solids*, Oxford University Press, Oxford ;;New York, 2001.

[16] J. Sipe, D. Moss, and H. van Driel, Physical Review B **35**, 1129 (1987).

[17] N. Bloembergen and P. Pershan, Physical Review **128**, 606 (1962).

[18] P. Guyot-Sionnest, W. Chen, and Y. Shen, Physical Review B **33**, 8254 (1986).

[19] V. Mizrahi and J. E. Sipe, Journal of the Optical Society of America B **5**, 660 (1988).

[20] G. Powell, J. Wang, and D. Aspnes, Physical Review B **65** (2002).

[21] B. S. Mendoza and W. L. Mochn, Physical Review B **55**, 2489 (1997).

[22] N. Arzate and B. Mendoza, Physical Review B **63** (2001).

[23] H. Peng and D. Aspnes, Physical Review B **70** (2004).

[24] C. Yamada and T. Kimura, Physical Review Letters **70**, 2344 (1993).

[25] C. Yamada and T. Kimura, Physical Review B **49**, 14372 (1994).

[26] S. Bergfeld and W. Daum, Physical Review Letters **90** (2003).

[27] O. A. Aktsipetrov, A. A. Fedyanin, V. N. Golovkina, and T. V. Murzina, Optics Letters **19**, 1450 (1994).

[28] C. Ohlhoff, G. Lpke, C. Meyer, and H. Kurz, Physical Review B **55**, 4596 (1997).

[29] T. Scheidt, E. Rohwer, H. von Bergmann, and H. Stafast, Physical Review B **69** (2004).

[30] V. Fomenko, E. P. Gusev, and E. Borguet, Journal of Applied Physics **97**, 083711 (2005).

[31] J. J. H. Gielis, B. Hoex, M. C. M. van de Sanden, and W. M. M. Kessels, Journal of Applied Physics **104**, 073701 (2008).

[32] J. Price, Y. Q. An, P. S. Lysaght, G. Bersuker, and M. C. Downer, Applied Physics Letters **95**, 052906 (2009).

[33] Y. V. White et al., Applied Physics Letters **88**, 062102 (2006).

[34] Y. Glinka et al., Physical Review B **65** (2002).

[35] B. Jun et al., Applied Physics Letters **85**, 3095 (2004).

[36] X. Lu et al., Physical Review B **78** (2008).

[37] S. A. Mitchell, R. Boukherroub, and S. Anderson, The Journal of Physical Chemistry B **104**, 7668 (2000).

[38] V. Fomenko, D. Bodlaki, C. Faler, and E. Borguet, The Journal of Chemical Physics **116**, 6745 (2002).

[39] **To be published**.

[40] N. Bloembergen, R. Chang, and C. Lee, Physical Review Letters **16**, 986 (1966).

[41] N. Bloembergen, R. Chang, S. Jha, and C. Lee, Physical Review **174**, 813 (1968).

[42] J. Dadap et al., Physical Review B **53**, R7607 (1996).

[43] J. I. Dadap, P. T. Wilson, M. H. Anderson, M. C. Downer, and M. ter Beek, Optics Letters **22**, 901 (1997).

[44] J. Mihaychuk, N. Shamir, and H. van Driel, Physical Review B **59**, 2164 (1999).

[45] T. Heinz, *Second-Order Nonlinear Optical Effects at Surfaces and Interfaces*, Elsevier, 1991.

[46] B. Koopmans, F. van der Woude, and G. Sawatzky, Physical Review B **46**, 12780 (1992).

[47] O. Aktsipetrov et al., Physical Review B **60**, 8924 (1999).

[48] R. Williams, Physical Review **140**, A569 (1965).

[49] V. Zubkov, J. Senosiain, S. Aronowitz, V. Sukharev, and C. Musgrave, Mater. Res. Soc. Symp. Proc **610**, B5.11.1 (2000).

[50] Y. Wu, H. Niimi, H. Yang, G. Lucovsky, and R. B. Fair, J. Vac. Sci. Technol. B **17**, 1813 (1999).

[51] M. Otani, K. Shiraishi, and A. Oshiyama, Physical Review Letters **90** (2003).

[52] M. Otani, K. Shiraishi, and A. Oshiyama, Physical Review B **68** (2003).

[53] S. Campbell, *The science and engineering of microelectronic fabrication*, Oxford University Press, New York, 2nd ed. edition, 2001.

[54] Q. Lu and T. K. Liu, Electrochemical and Solid-State Letters **9**, G296 (2006).

[55] S. Markov et al., physica status solidi (a) **205**, 1290 (2008).